Inferring Monosynaptic Connectivity Across Brain Structures In-Vivo

Yi Juin Liew[1], Aurélie Pala[1], Clarissa J Whitmire[1], William A Stoy[1],

Craig R Forest [1,2], Garrett B Stanley[1]

[1]Wallace H Coulter Department of Biomedical Engineering, Georgia Institute of Technology and Emory University, Atlanta, GA, USA

[2]George W Woodruff School of Mechanical Engineering, Georgia Institute of Technology, Atlanta, GA, USA

Abbreviated title: Inferring monosynaptic connectivity in vivo

With 39 text pages, 7 figures, 2 supplemental figures

Correspondence: Garrett B Stanley
Coulter Department of Biomedical Engineering
Georgia Institute of Technology & Emory University
313 Ferst Dr
Atlanta GA 30332-0535
USA

Phone: 404-385-5037
Fax: 404-385-5044
Email: garrett.stanley@bme.gatech.edu

Keywords: thalamocortical; cross correlation; signal detection; causality; inference

Disclosures: The authors declare no competing financial interests.

Acknowledgements: This work was supported by NIH/NIMH Brain Initiative Grant U01MH106027 (GBS and CRF) and NIH/NINDS Brain Initiative Grant R01NS104928 (GBS). YL was supported by a Georgia Tech-Emory-PKU Global Biomedical Engineering Fellowship. AP was supported by a Swiss National Science Foundation (SNSF) Advanced Postdoc Fellow. CJW was supported by an NIH NRSA Pre-doctoral Fellowship. WAS is supported by an NSF Graduate Research Fellowship.

Abstract/Summary:

As the tools to simultaneously record electrophysiological signals from large numbers of neurons within and across brain regions become increasingly available, this opens up for the first time the possibility of establishing the details of causal relationships between monosynaptically connected neurons and the patterns of neural activation that underlie perception and behavior. Although recorded activity across synaptically connected neurons has served as the cornerstone for much of what we know about synaptic transmission and plasticity, this has largely been relegated to *ex-vivo* preparations that enable precise targeting under relatively well-controlled conditions. Analogous studies *in-vivo*, where image-guided targeting is often not yet possible, rely on indirect, data-driven measures, and as a result such studies have been sparse and the dependence upon important experimental parameters has not been well studied. Here, using in-vivo extracellular single unit recordings in the topographically aligned rodent thalamocortical pathway, we sought to establish a general experimental and computational framework for inferring synaptic connectivity. Specifically, attacking this problem within a statistical signal-detection framework utilizing experimentally recorded data in the ventral-posterior medial (VPm) region of the thalamus and the homologous region in layer 4 of primary somatosensory cortex (S1) revealed a trade-off between network activity levels needed for the data-driven inference and synchronization of nearby neurons within the population that result in masking of synaptic relationships. Taken together, we provide a framework for establishing connectivity in multi-site, multi-electrode recordings based on statistical inference, setting the stage for large-scale assessment of synaptic connectivity within and across brain structures.

New & Noteworthy:

Despite the fact that all brain function relies on the long-range transfer of information across different regions, the tools enabling us to measure connectivity across brain structures are lacking. Here, we provide a statistical framework for identifying and assessing potential monosynaptic connectivity across neuronal circuits from population spiking activity that generalizes to large-scale recording technologies that will help us to better understand the signaling within networks that underlies perception and behavior.

Introduction

Every aspect of brain function, from sensory and motor processing, to memory and cognition, involves complex circuitry and communication across many different brain areas. Despite this fact, what we know about brain function has been derived largely from electrophysiological recordings targeted at single regions, and upon gross anatomical connection patterns across brain regions without specific precise knowledge of synaptic connectivity. Ultimately, understanding the causal interaction of neuronal dynamics that underlie perception and behavior requires ground truth evidence for synaptic connectivity that necessitates intracellular access to both pre- and post-synaptic neurons. Despite exciting advancement of a range of recording technologies such as simultaneous multi-neuron intracellular recordings in-vivo (Jouhanneau and Poulet 2019; Kodandaramaiah et al. 2018) and deep structure targeted patching (Stoy et al. 2017), targeting connections in-vivo using intracellular approaches remains a labor-intensive endeavour, is ultimately limited to a very small number of neurons, and does not scale to the circuit level. Extracellular recordings offer solutions to some of these issues, and thus offer promise in this direction.

The field of neuroscience is now at a time where large-scale recordings of neuronal populations at cellular resolution are possible across brain structures, due to the development of multi-electrode recording technologies such as 'Neuronexus' (Berényi et al. 2014; Buzsáki et al. 2015) (NeuroNexus Inc.), 'Neuropixels' (Jun et al. 2017), 'NeuroSeeker' (Fiáth et al. 2018; Raducanu et al. 2016)), and 3D silicon probes (Rios et al. 2016). These technologies provide access to surveying network level information flow, driving a growing need for a rigorous experimental and analytic framework to identify functional relationships across brain structures. In previous studies, in-vivo approaches to establishing synaptic connectivity across recorded pairs of neurons have been developed based on analytic methods applied to recorded spiking data (Nowak and J 2000; Perkel et al. 1967), historically conducted in larger animals such as cats, rabbits, and rats (Reid and Alonso 1995; Swadlow and Gusev 2001; Wang et al. 2010) and only more recently in mouse (Lien and Scanziani 2018). Approaches based on spike correlations are the most common for quantifying functional interactions and inferring monosynaptic connections in-vivo. These approaches have been utilized in paired recording studies that involved measuring correlation in the spiking activity between neurons (Barthó et al. 2004; Csicsvari et al. 1998; English et al. 2017; Fujisawa et al. 2008; Reid and Alonso 1995; Swadlow and Gusev 2001; Wang et al. 2010) or between the spiking activity of a pre-synaptic neuron and the subthreshold membrane potential of a putative post-synaptic target (Bruno and Sakmann 2006; Matsumura et al. 1996) (London et al. 2010; Sedigh-Sarvestani et al. 2017; Yu and Ferster 2013). Correlational

approaches are statistical in nature and thus have been anecdotally reported to be strongly dependent upon data length and are very sensitive to a range of possible confounds, but a comprehensive understanding of these relationships and a unified approach are both lacking.

Here, using the thalamocortical circuit in rodents as a model system, we establish methodological strategies for extracellular, topographically aligned in-vivo single-unit recordings in thalamus and cortex for both rat and mouse. This analytic framework for inferring connectivity is based on signal-detection theory, and directly addresses issues of data length dependence and confounds produced by population synchrony. Specifically, we outline a work-flow of topographic mapping and histological validation, followed by a statistical approach for signal-detection based classification of putative connected and non-connected pairs with an assessment of classification confidence that is scalable to the large-scale recording approaches that are emerging in the field. We found that while the amount of spiking was a strong determinant of the accuracy of the inference of connectivity, there was an important tradeoff between the activity in the network and the underlying population synchrony that regulates the likelihood of both discovering a synaptic connection that is present and correctly classifying unconnected pairs as such. Taken together, we provide a data-driven framework for inferring connectivity and the corresponding statistical confidence that generalizes to large-scale recordings across brain structures.

METHODS

Animals

Twelve female adult Sprague Dawley rats (225-330g) and two male C57BL/6 mice were used in all the experiments. All procedures were approved by the Georgia Institute of Technology Institutional Animal Care and Use Committee and followed guidelines established by the National Institutes of Health. Note that there were some major differences in animal preparation, surgery and craniotomies as well as electrophysiology for rat and mouse, as described below. However, procedures such as whisker stimulation, post-mortem histology, and analytical methods used for analysis were largely identical.

Animal preparation, surgery and craniotomies.

*Rat***.** Animals were first sedated with 5% vaporized isoflurane and maintained at 3% vaporized isoflurane when transitioned to fentanyl-cocktail anesthesia via tail vein injection. Fentanyl cocktail anesthesia (fentanyl [5 µg/kg], midazolam [2 mg/kg], and dexmedetomidine [150 mg/kg])) was administered continuously via a drug pump at an initial rate of 4.5 uL/min (Ahissar et al. 2000; Whitmire et al. 2016). During the transition, anesthesia level was monitored closely by measurement of heart rate and respiratory rate. Body temperature was maintained at 37 °C by a servo-controlled heating pad. Under the effect of both anesthetic agents, the animal's heart rate tended to decrease gradually over several minutes. The isoflurane level was then titrated down in 0.5% decrements during the transition to the fentanyl cocktail. Upon successful transition, which ranged from 5-15 min depending on the animal, the heart rate was targeted for approximately 240 -270 bpm. After the effects of fentanyl cocktail stabilized (in terms of heart rate) and the animals showed no toe pinch response, the animals were then fixed in the stereotaxic device by securing the head of the animal in place with ear bars on a floating table in an electromagnetically shielded surgery suite. The position of the ear bars was verified with uniform eye levels and usually with eardrum penetration on both sides of the head. Eye ointment (Puralube Vet Ointment) was applied to prevent the animal's eyes from dehydration. An incision was made along the midline of the skull, and skin was removed for visibility of bregma and lambda (Paxinos and Watson 2007). Connective tissue and muscle that were close to the ridge of the skull were detached and removed to expose the skull surface that was directly above the barrel cortex. To ensure that the skull remained level throughout the recording, the height of the skull surface was measured at bregma and lambda, and the difference was minimized (< 200 um) by adjusting the angle of the head with the nose cone position.

We made two craniotomies on the animal's left hemisphere above the ventro-posteromedial nucleus (VPm) and the S1 barrel cortex based on stereotaxic coordinates. For the cortical craniotomy, which usually extended over the ridge of the skull, the

168 stereotaxic device was rotated to an angle (~40° relative to vertical) for better visualization
169 and drilling. Both craniotomies were drilled slowly until the skull piece appeared to be
170 floating and mobile. We irrigated the skull surface periodically with Ringer's solution when
171 drilling to remove debris and prevent overheating from drilling. Before removing the skull
172 piece to expose the cortex, a small dental cement reservoir was carefully built around the
173 craniotomies to hold the Ringer's solution for irrigation and to keep the recording site
174 continually moist. The lateral side of the wall was built thicker and higher due to the
175 curvature of the skull toward the ridge. To provide strong adherence to the skull,
176 cyanoacrylate containing adhesive (Krazy Glue, Elmer's Products Inc.) was carefully
177 applied around the external edges of the reservoir, leaving the bregma and major skull
178 sutures visible at all times. For grounding purposes, another hole with ~0.5 mm diameter
179 was drilled (Henry Schein, Carbide Burr HP 2) on the right hemisphere of the skull and
180 fastened with a skull screw and a metal wire. The skull pieces at both recording sites
181 were then carefully removed with forceps (FST Dumont #5/45). To minimize brain
182 swelling, the dura was left intact on both recording surfaces, and warm Ringer's solution
183 was repeatedly added and absorbed with cotton tips until the blood was cleared. An
184 absorbent gelatin compressed sponge (Gelfoam, Pfizer Inc.) was sometimes used to
185 clear the blood.
186
187 *Mouse*. Head-plate implantation and intrinsic imaging procedure were usually performed
188 at least three days to one week before acute experiment. A lightweight custom metal
189 (titanium or stainless steel) head-plate was implanted on the skull of the mouse for head
190 fixation and improved stability during recording, in accordance with a previously described
191 protocol (Borden et al. 2017). During this survival surgical preparation, the animal was
192 sedated with 5% vaporized isoflurane and anesthesia was maintained with 2-3%
193 isoflurane for the head-plate procedure. We administered opioid and non-steroidal anti-
194 inflammatory analgesic (SR-Buprenorphine 0.8 - 1 mg/kg, SC, pre-operatively, and
195 Ketoprofen 5-10 mg/kg, IP, post-operatively) and covered the animal's eyes with
196 ophthalmic eye ointment (Puralube Vet Ointment). Body temperature was monitored and
197 maintained at 37 °C. After sterilizing the skin above the skull and applying topical
198 anesthetic (lidocaine 2%, 0.05 ml, max 7mg/kg, SC), we removed the skin and scraped
199 off periosteum and any conjunctive tissue off the skull. We gently separated tissue and
200 muscles close to the lateral edge of the skull using a scalpel blade (Glass Van &
201 Technocut, size no. 15), leaving sufficient room for head-plate attachment and away from
202 targeted recording areas. To ensure that the skull surface remained level during head
203 fixation, we adjusted animal's head position to minimize the relative height difference (<
204 150 um) between the skull surface at the bregma and lambda landmarks (Franklin and
205 Paxinos 2008). We found this step to be critical especially for VPm targeting. We secured
206 the metal headplate over the intact skull with C&B-Metabond (Parkell Prod Inc) and skin

adhesive (Loctite 401, Henkel). The Metabond dental acrylic was chilled using ice, slowly applied to the skull surface, and allowed to cure for 5-10 minutes before we covered the rest of the attachment site and edges of the skin incision with skin adhesive (Loctite 401) to ensure that the skin edges were securely adhered to the skull. The final head-plate and dental acrylic structure created a recording well for holding Ringer solution (in mM: 135 NaCl, 5 KCl, 5 HEPES, 1 $MgCl_2$-$6H_2O$, 1.8 $CaCl_2$-$2H_2O$l pH 7.3) for future imaging and electrophysiological recording sessions. For grounding purposes, another hole with ~0.5 mm diameter was drilled (Henry Schein, Carbide Burr HP 2) on the right hemisphere of the skull and fastened with a skull screw (Miniature Self-Tapping Screws, J. I. Morrisco). A metal wire was connected to the skull screw on the day of recording to serve as animal ground. We applied a thin layer of transparent glue (Loctite 401, Henkel) over the left hemisphere to protect the skull and covered the exposed skull with a silicone elastomer (Kwik-Cast, World Precision Instruments) if there were no other additional procedures after head-plate implantation.

Intrinsic Optical Imaging in the Mouse S1 Barrel Cortex. We performed intrinsic signal optical imaging of whisker-evoked responses in mouse primary somatosensory cortex under 1-1.2% isoflurane anesthesia to functionally identify individual barrel columns (Lefort et al., 2009; Pala et al., 2015). All whiskers except the whiskers of interest (A2, B1, C2, D1, D3 and E2) were trimmed. We thinned the skull using a dental drill (0.1 mm diameter bit, Komet, USA) until blood vessels became visible. We applied warm Ringer's solution on top of the skull and covered it with a glass coverslip (thickness 0.13-0.17mm, Fisherbrand). We captured a reference image of the blood vasculature under green illumination (530nm) (M530F1 LED, Thorlabs). We delivered repetitive whisker stimuli (10 Hz, sawtooth pulses, 1000 deg/s) to individual whiskers using a galvanometer system (Cambridge Technologies) while performing imaging on barrel cortex under red illumination (625 nm) (M625F1 LED, Thorlabs) – see Whisker Stimulation section below. Images were acquired using a CCD Camera (MiCam02HR, SciMedia) at 10 Hz, with a field of view of approximately 4 x 2.5 mm, corresponding to 384 x 256 pixels (resolution: 100pixel/mm). Each trial lasted 10s, with 4s of baseline followed by 4s of whisker stimulation and 2s without stimulation. The inter-trial interval was 30s. Whisker-evoked responses were averaged over 10-20 trials. Intrinsic signals were measured as the relative change in reflectance by taking the overall mean reflectance during whisker stimulation (R_{stim}) and subtracted the mean baseline reflectance (R_{stim} - $R_{baseline}$). Acquisition and processing of the images were implemented using "BV_Ana" software (MiCam02HR, SciMedia, Ltd) and Matlab (MathWorks, Natick, 2015). We recorded intrinsic signals from at least three barrels and estimated location of the unmapped barrels by overlaying a template barrel map reconstructed from histology. At the end of the imaging session, we applied transparent glue (Loctite 401) directly on the S1 site to

protect the thinned skull from contamination and infection and sealed the exposed skull with a silicone elastomer (Kwik-Cast, World Precision Instruments).

On the day of recording, the head of the mouse was held in place with a head-post clamp and animal should remain in the flat skull position. We covered the eyes with ophthalmic eye ointment (Puralube Vet Ointment) to prevent dehydration. The animal was then anesthetized using 2-3% isoflurane. Before performing the craniotomies, we thinned the skull above VPm and S1 layer-by-layer with a dental drill (0.1 mm diameter bit, Komet, USA) and irrigated the skull surface with Ringer's solution frequently to remove debris and prevent overheating. When the skull was thin enough to easily puncture, we made two small craniotomies above VPm (approximately 1 mm diameter; centered at 1.8 mm caudal and 1.8 mm lateral to bregma) and S1 (approximately 0.5 mm diameter, using the intrinsic imaging signal and the blood vasculature as a landmark) by penetrating the thinned skull using an insulin syringe needle tip (at about 40-50 degree angle) to make small holes outlining the edges of the craniotomies until the circular skull piece was loosely attached. The less perforated region of the circular skull piece was used as a pivot, and we levered the skull pieces off from the more perforated edge using fine-tip forceps (FST Dumont #5SF) to expose the brain surface.

Electrophysiology

Neuronal recordings. Tungsten microelectrodes (FHC, impedance: 2-5 MΩ, 75 μm in diameter) were used in thalamus and cortex to isolate single units that were responding to a single primary whisker on the contralateral side of the face. Multielectrode silicon probes with 32 recording sites (A1x32-Poly3-5mm-25s-177 or A1x32-Poly2-10mm-50s-177, NeuroNexus) were also independently lowered into the thalamus and cortex. Note that tungsten microelectrodes were used in rat studies and probe recordings were used in mouse studies. Data were collected using a 64-channel electrophysiological data-acquisition system (TDT Model, etc. RZ2 Bioprocessor). Neuronal signals were amplified, and bandpass filtered (500Hz-5kHz) and digitized at ~25kHz per channel. Stimulus waveform and other continuous data were digitized at 10kHz per channel. Simultaneously, the local field potential (LFP) signal were obtained by using a 0.5-200Hz bandpass filter. The LFPs were used to identify primary whisker response (see Whisker Stimulation).

Rat. VPm recordings. We targeted the VPm region of the thalamus by advancing a single tungsten microelectrode (FHC, 2 MOhm impedance) perpendicular to the pial surface into the thalamic craniotomy centered at 3.0 mm caudal and 3.0 mm lateral to bregma. We quickly advanced (~50um/s) to the depth of 4000 μm and slowed down to the speed of ~3 μm/s while searching for responsive cells by manually deflecting the whisker on the contralateral side of the vibrissal pad. Whisker responsive cells were typically located at

285 a depth of 4800-5300 μm, measured using a precision micromanipulator (Luigs &
286 Neumann, Germany). *S1 recordings*. At a position 5.8 mm lateral and 2.5 mm caudal to
287 bregma, we inserted a single tungsten microelectrode at an angle of 40-45° (relative to
288 the vertical axis of electrode holder). We positioned the tip of the electrode gently touching
289 the dura and advanced slowly to create an opening in the membrane. The microelectrode
290 was then slowly advanced into cortical tissue at a speed of ~3 μm/s (measured at 1μm
291 resolution). All cortical units were recorded at stereotaxic depths of 700-1000μm,
292 corresponding to layer IV of rat barrel cortex based on literature (Bruno and Sakmann
293 2006; Constantinople and Bruno 2013).
294
295 *Mouse. VPm recordings.* For first penetration, electrode was typically lowered at 1.8 mm
296 caudal and 1.8 mm lateral to bregma. If we could not functionally locate VPm using this
297 method, we used the relative distance from the location of barrel cortex (usually measured
298 1.0-1.2mm from the B1 or Beta barrel column to find whisker responsive thalamic regions).
299 For probe recordings, we searched for whisker responsive cells by manual whisker
300 deflection using the deepest channel as reference. We typically found whisker responsive
301 cells were at a depth between 2800um-3200 um. *S1 recordings.* Based on intrinsic
302 imaging signal, a small craniotomy (diameter ~0.5 mm) was created at the desired
303 location on the barrel cortex that was distant from blood vessels. We positioned the
304 electrode at a 35 ° angle from the vertical axis (parallel to the barrel column) and recorded
305 from cortical neurons at a stereotaxic depth of 300-500um from the cortical surface.
306
307 **Whisker Stimulation**
308 To identify the single whisker of interest, we first manually deflected all whiskers on the
309 vibrissal pad while monitoring the extracellular signal. Once units were isolated by moving
310 the electrode as close as possible to the responsive cells that primarily responded to
311 single whisker, we delivered controlled, single whisker stimulation in the rostral-caudal
312 plane using a computer-controlled actuator, galvo-motor (galvanometer optical scanner
313 model 6210H, Cambridge Technology). Whiskers were trimmed ~12 mm from the face.
314 Primary whisker (PW) was defined as whisker deflection that evoked the maximal
315 neuronal response with shortest latency (see Transient Stimulus). The primary whisker
316 was fed into the insertion hole at the end of an extension tube (inner diameter: ~200-300
317 μm um, length: 15mm) that was connected to the rotor of the galvanometer stimulator.
318 The stimulus probe was positioned at 10 mm from the vibrissal pad. The range of motion
319 of the galvanometer was ±20°, with a bandwidth of 200Hz. The galvanometer system was
320 controlled using a custom developed hardware/software system (Matlab Real-Time
321 Simulink System, MathWorks). Whisker evoked responses were measured using raster
322 plots and peri-stimulus time histograms (PSTH, 1-ms bin resolution) across trials.
323

Transient stimulus. For mapping whisker receptive field at the recording sites, we presented high velocity (600 or 1000 °/s) rostral-caudal whisker deflection to evoke reliable whisker responses. Trains of solo pulses, followed by a separate, pulsatile adapting stimulus at 8-10 Hz (Borden et al. 2017; Whitmire et al. 2016) were delivered for 60-100 times. To measure whisker response to different stimulus strength, pulses with angular deflection velocities of 50, 125, 300, 600, 900, 1200 deg/s were presented randomly. Rostral-caudal pulse deflections were either a Gaussian-shaped deflection waveform or a simple exponential sawtooth (rise and fall time = 8 ms). We quantified whisker evoked activity 30 ms after stimulus onset and then further characterized onset latencies of first spike within the response window in response to non-adapting solo pulses and adapting pulsatile stimuli over 60-100 trials. Mean first spike latencies, defined as the average time delay between stimulus onset and the first spike in the response window after stimulus presentation. This metric was used for all thalamic and cortical units. For 32-channel probe recording in thalamus, we quantified the LFP response in a 30 ms post-stimulus window for each channel to identify principal whiskers (PW). Well-isolated single units that showed whisker responsiveness was verified by calculating LFP peak amplitude and peak latency to different whisker stimulation.

A neuronal pair was verified to be topographical aligned when they (1) shared maximum response (SUs max FR and LFP amplitude) to the same primary whisker under punctate stimulation and (2) latency difference of whisker response within 1-5 ms delay (LFP peak latency and SU mean FSL, or SU mean peak latency).

Weak sinusoidal stimulus. For monosynaptic connection quantification, we probed the thalamocortical circuit using a weak, desynchronizing sinusoidal whisker stimulus to elevate baseline firing rates in recorded units. We delivered 4°, 2-4Hz weak sinusoidal deflections (Bruno and Sakmann 2006; Bruno and Simons 2002; Wang et al. 2010) for approximately 200-500 trials to obtain at least 2000 spikes for the cross-correlation analysis. Occasionally, we eliminated the first 0.5-1 s of the trials due to high firing rate at the onset of stimulus presentation.

Post-mortem Histology

In order to verify recording sites and the angle of penetration that was optimal for locating VPm and S1, we perfused a small subset of animals after the paired recording experiment. To label each electrode recording track, we slowly retracted the electrode along its axis of entry at the conclusion of recording and applied a few drops of DiI (2.5mg/mL, in ethanol). We then reinserted the electrode into the same penetration site and back along the same axis and left the electrode in the brain for at least 15 minutes. Following the end of the experiment, we euthanized the animal with an overdose of sodium pentobarbital

363 (euthasol, 0.5 mL at 390mg/mL for rat, 0.1 mL at 390 mg/mL), performed a transcardial
364 perfusion, extracted the brain, and fixed the brain in 4% paraformaldehyde (PFA, Electron
365 Microscopy Sciences) overnight. We sliced the brain in 100 um coronal sections and
366 performed cytochrome oxidase staining to reveal VPm (barreloid) and S1 (barrel). As an
367 additional verification of recording site, we identified the overlap between the DiI stained
368 recording track and the CO-stained regions.
369
370 **Analytical Methods**
371 *Extracellular spike sorting.* In assessing potential synaptic connectivity using cross-
372 correlation analysis, the clear isolation of single unit activity from extracellularly recorded
373 voltage signals is particular critical. In all of our paired recording experiments, we
374 performed extracellular single-unit recordings using either Tungsten microelectrodes or
375 32-channel NeuroNexus probes. Although similar in approach, the sorting of recorded
376 data into single-units was implemented using different softwares. For the single micro-
377 electrodes, we performed spike sorting offline using the Plexon Offline Sorter (Plexon Inc,
378 Dallas TX, USA), while for the 32-channel probe recordings we utilized the KlustaKwik
379 and KiloSort software package (Harris et al. 2000) .
380
381 Tungsten microelectrode: For high quality single unit recordings, we classified the
382 recordings as single units if they fulfilled the following criteria: (1) high signal-to-noise ratio
383 (SNR): Peak-to-peak amplitude of spike waveforms greater than four standard deviation
384 of the background signal. Standard deviation of the background noise was calculated
385 with a robust estimator, median (|V|)/0.6745 by randomly selecting five 1s segments of
386 raw continuous voltage traces (Rossant et al. 2016). (2) High waveform unit quality
387 (UQ>3), defined as mean peak-to-peak voltage (Vpp) divided by 2 times mean standard
388 deviation (SD) of the waveform. (3) Had less than 1% refractory period violation of the
389 total spikes. Neuronexus 32-channel probe: Well-isolated single units were classified
390 using the following criterions. (1) Unit Quality >3, has ISI violation less than 1.
391
392 *VPm unit verification:* It is important to distinguish different thalamic nuclei from one
393 another, and particularly so in the mouse, where the regions are very small and very close
394 together. After recording, we used a combination of measures to distinguish VPm from
395 PoM thalamic units: (1) Average first-spike latency to punctate (non-adapting) stimuli,
396 quantifying the average time taken for somatosensory information to be transmitted along
397 the lemniscal pathway to thalamus (Whitmire et al. 2017). (2) Shift in average first-spike
398 latency response to adapting stimuli, defined as the time difference between average
399 response to the first adapting stimulus and last adapting stimulus.
400

Cortical unit classification. It was known that S1 layer IV is the major thalamocortical recipient from VPm projections and there exist some heterogeneity in terms of cortical cell types in Layer IV (Bruno and Simons 2002). Here, we classified cortical units into fast-spiking unit (FSU) and regular-spiking unit (RSU) by using waveform parameter. We quantified the time interval between trough to peak (t_{t2p}) of the spike waveform (Barthó et al. 2004).

Cross-correlation analysis. All analysis was performed in a trial-by-trial basis. Given a spike in a 'reference' neuron, we computed the relative times of the spikes from a 'target' neuron that occurred within a 25-millisecond window before and after each reference spike. Cross-correlograms were constructed using 0.5 milliseconds bin. For monosynaptic connectivity inference, we used thalamic spiking as reference and cortical spiking as target and examined correlated firing within 1-4 ms lag. To measure the level of presynaptic synchronization in thalamus, we performed a cross-correlation analysis on all thalamic pairs that responded to the same principal whisker that was identified using local field potential (LFP) and single units (SUs). Thalamic synchrony was measured for each thalamic pair using number of spikes within a ± 7.5 ms window of the cross-correlogram normalized by the number of spikes from each neuron (Wang et al. 2010; Whitmire et al. 2016).

Probabilistic measure of connectivity inference. For each pair of thalamocortical neurons, we repeated the cross-correlational analysis with bootstrapping method. This was done by performing resampling on the dataset with replacement, with approximately 500-1000 iterations for each condition. By counting the number of iterations that fulfil each criterion, this resulted in a p-value that can be attached to the binary classification of monosynaptic connection.

Data-length effect on the connectivity metric. Simulation for various data-lengths was implemented by using subsamples (in unit of trials) of VPm and S1 spikes for cross-correlation analysis. For each data-length condition, we computed the resampled peak height, h*. A bootstrapped estimator of bias was computed as the difference between the mean of the resampled peak height and the original metric, assuming a normal distribution:

$$bias = E(h^* - h)$$

Where E(.) denotes statistical expectation. The variance was estimated as the square of the resampled peak height:

$$variance = var(h^*)$$

A significance level for the inference for a 'putatively connected' pair was computed and denoted as the probability of a hit when the peak height metric for the resampled data exceeded the criterion for the inference of a functional connection. The probability of a miss is complementary:

$$P(hit) = \frac{\#\{h^* \geq criterion\}}{\#\ of\ iterations}, \qquad criterion = 3.5$$

$$P(miss) = 1 - P(hit)$$

On the other hand, the significance level for a 'not connected' pair was computed and denoted as the probability of a correct reject when the peak height metric for the resampled data is less than the criterion.

$$P(correct\ reject) = \frac{\#\{h^* < criterion\}}{\#\ of\ iterations}, \ \ criterion = 3.5$$

$$P(false\ alarm) = 1 - P(correct\ reject)$$

<u>Thalamic synchrony effect on connectivity metric.</u> Simulation for various thalamic synchrony level was implemented by manipulating both firing rate and spike timing of VPm and S1. Given that both firing rate and thalamic synchrony were affected with increasing stimulus strength, our simulation was conducted using data that was collected under spontaneous condition. For a connected pair, we set the ratio between VPm and S1 firing to be constant at each synchrony level for simplification. However, we systematically increased spiking activity (in number of spikes per trial) in VPm and S1 with a specific amount of jitter (zero-mean Gaussian noise of a specific standard deviation, sigma) as a function of thalamic synchrony. For a not-connected pair, the increase in thalamic synchrony and VPm and S1 firing were simulated by systematically adding spikes from another pair of neurons that is putatively connected. The assumption here was that a not-connected pair would become more identical to its neighboring neuron (that has a functional connection to the downstream S1 neuron) with increasing synchrony. This was repeated from 100-500 iterations for each synchrony level and the probability of satisfying Criterion 1 and 2 was computed.

Results

Here, we present a comprehensive experimental and analytic framework for assessing synaptic connectivity using extra-cellular spiking activity from simultaneously recorded single units across brain structures. First, we provide a rigorous experimental protocol for performing simultaneous single-unit electrophysiological recording in topographically aligned regions in the thalamocortical circuit of the somatosensory pathway using a combination of stereotaxic targeting based on anatomical landmarks, sensory-evoked response properties, and post-hoc histological validation. We highlight some similarities and differences of the technical aspects of paired recordings performed in rats versus mice, two commonly used rodent species in mammalian electrophysiology. Next, we generate inferences regarding the synaptic connectivity of two single units based on spike correlation analysis across the presynaptic VPm and postsynaptic S1 spiking, leading to classification as either "connected" or "not connected", using an approach to be explained in detail below. Figure 1A highlights the basic experimental setup and analysis utilized in this study, with electrophysiological recordings targeted to primary somatosensory "barrel" cortex (S1, red) and to ventro-posteromedial thalamus (VPm, blue), during controlled deflections of a single whisker on the contralateral side of the face with a computer-controlled actuator (see Methods). In the context of a signal detection framework, we then quantify the effects of experimental data-length and local synchrony of presynaptic neurons on monosynaptic connection inference, and importantly, expand this framework to attach statistical levels of confidence to the synaptic connectivity inferences.

Experimental workflow to establish paired recordings

Paired recordings in topographically aligned feedforward sensory regions in-vivo have been previously shown to be experimentally tractable (Bruno and Sakmann 2006; Bruno and Simons 2002; Reid and Alonso 1995; Swadlow and Gusev 2001; Wang et al. 2010) yet it remains a challenging process, and to our knowledge, detailed reports on experimental approaches have not been published in full. Here, we documented the steps in details. Figure 1B summarizes the general workflow for establishing and analyzing paired recording: 1) mapping primary somatosensory cortex (S1), 2) localizing the ventral posteromedial (VPm) nucleus of the thalamus, 3) achieving and verifying topographical alignment of recording electrodes across VPm and S1, 4) connectivity assessment through statistical analysis of the measured spiking activity from pairs of single-units across recording sites, and 5) histological verification of recording site locations.

Although the final electrode placement for paired recording involved thalamic electrode placement followed by placement of the cortical electrode, we found that an initial

516 somatotopic mapping of cortex was critical for efficiently achieving topographical
517 alignment. As part of the approach, we thus first performed coarse cortical mapping prior
518 to thalamic localization. In rat, we employed primarily electrophysiological mapping
519 approaches for this coarse mapping of S1. We targeted S1 using approximate stereotaxic
520 coordinates and inserted a single electrode to obtain the functional location of several
521 "barrels" using bregma as a reference point. Once we located the S1 region, we identified
522 the stereotaxic location of three barrel columns containing neurons that were responsive
523 to the movement of single primary whiskers (See Supplementary Figure 1 -
524 https://doi.org/10.6084/m9.figshare.13075940.v1). We used this relative distance
525 between columns/barrels to estimate the overall topography of S1 by overlaying a barrel
526 map template scaled to fit the three data points. In mouse, taking advantage of the optical
527 properties of the mouse skull (i.e. that it is relatively translucent), we employed intrinsic
528 optical signal imaging (IOS) for the coarse cortical mapping. Intrinsic optical signals were
529 acquired in response to separate, punctate deflections of three different single vibrissae.
530 The corresponding cortical regions of activation were co-registered with the anatomy of
531 the blood vessels and further used as a landmark for electrode placement. This
532 triangulation methodology was adapted from our laboratory previously published method
533 (Gollnick et al. 2016; Millard and Stanley 2013). An example of this is shown in Figure 2A.
534 The three images on the top row were acquired in response to punctate deflections of the
535 Beta whisker (wBeta), the C2 whisker (wC2), and the B2 whisker (wB2), respectively.
536 Each image represents the mean 0- to 6-s post-stimulus response (baseline subtracted
537 and scaled) to a 4-s 10-Hz 1000 deg/s pulsatile stimulus, with the region of cortical
538 activation appearing as a dark spot near the center of the image, at different locations for
539 each whisker. We then fitted a barrel map template, recovered from histological brain
540 sections from previous experiments onto the overall optical image of the brain surface
541 through the thinned skull (template shown in bottom left of Figure 2A). The three centroids
542 of the intrinsic imaging signals were used as reference points (Figure 2A, bottom middle)
543 for transformation of the barrel map template involving scaling, rotation, translation and
544 shearing. This transformed map along with the blood vessel image (Figure 2A, bottom
545 right) was then used as a navigation guide for electrode placement for targeting a desired
546 barrel column.
547
548 Once the cortex was coarsely mapped using the above approaches, we inserted an
549 electrode to localize VPm (see Method: Electrophysiology). Specifically, we identified
550 specific thalamic barreloids by manually deflecting each of the facial vibrissae individually
551 in order to find an isolated unit that was maximally responsive to a single whisker only.
552 Note that the procedure was nearly identical for rat and mouse, except that for the mouse,
553 a silicon multi-electrode probe was utilized, and localization was performed using one of
554 the probe sites, usually the deepest probe contact. Given that the probe was spanning

555 several hundred microns on the thalamic recording site, we typically recorded from one
556 to three barreloids simultaneously with two or more recording sites within a single
557 barreloid. Final placement of the electrode was fixed when well-isolated units were
558 detected on probe contacts. For verification of barreloid targeting within VPm, we
559 compared local field potential (LFP) responses to individual stimulation of multiple nearby
560 vibrissae. Figure 2B shows an example of LFPs recorded in the A3 barreloid of thalamus
561 on one of the probe contacts. Note that the evoked LFP response exhibits an initial
562 negative peak for the whisker A3 deflection (wA3, blue) that is substantially larger than
563 responses to the deflection of other whiskers.
564
565 A practical challenge lies in the positioning of the recording electrodes to reach the
566 multiple target areas. In a small subset of experiments, we optimized the electrode
567 insertion angle by coating the electrodes with fluorescent dye (DiI) to mark the electrode
568 track for post-experiment histological analysis. A range of insertion angles was tested for
569 both S1 and VPm in mouse and rat. We found that the optimal electrode angle to target
570 VPm thalamus in both rats and mice was 0 degrees from vertical (perpendicular to the
571 brain surface) (Figure 2C and Supplementary Figure 1 -
572 https://doi.org/10.6084/m9.figshare.13075940.v1). For S1 targeting, we found that the
573 optimal angle for rats was approximately 40-45 degrees from vertical and was
574 approximately 30-35 degrees from vertical for mice (Figure 2C) for electrode penetration
575 parallel to the cortical column/barrel, important for accurate targeting of specific cortical
576 depths. The target recording site depths were determined based on published anatomical
577 locations of the target structures (see Methods). Figure 2C shows typical electrode tracks
578 targeting S1 and VPm in a mouse (left), along with the corresponding raw extracellular
579 recordings from one VPm and one S1 electrode recording site. Both the VPm and S1
580 extracellular recordings show sensory driven responses to deflections of the same
581 whisker, the pattern of which is shown in the extracellular recordings of Figure 2C. The
582 times of whisker stimulation are denoted with the green arrows, representing a pattern of
583 two isolated whisker deflections, followed by an 8 Hz train of whisker deflections. The
584 raw electrophysiological recordings were subsequently sorted into single-unit data based
585 on conventional spike sorting approaches and only well-isolated units were retained for
586 analysis (see Methods).
587
588 **Sensory response in topographically aligned VPm – S1 layer 4 regions**
589 Achieving topographically aligned recordings across corresponding thalamic barreloids
590 and cortical barrel columns necessitates the accurate targeting of the thalamic recording
591 electrode/probe to the VPm nucleus of the thalamus. In particular, it is key to be able to
592 distinguish whisker-responsive units located in VPm from those located in the adjacent
593 posteromedial nucleus (POm) of the thalamus. In previous studies, POm units have been

shown to have multi-vibrissae receptive fields, responding to approximately six vibrissae on average, ranging from three to twelve whiskers (Castejon et al. 2016; Diamond et al. 1992). Hence, to ensure recordings from VPm neurons, we selected thalamic units that only had restricted whisker sensitivity, usually only to one principal whisker (as previously shown in Figure 2B, VPm targeting (LFP)). Furthermore, VPm neurons have been shown to have shorter response latency than POm neurons (Ahissar et al. 2000; Landisman and Connors 2007). The thalamic single units kept for subsequent connectivity analysis had strong response to a punctate whisker stimulus with short latency (8.12 ms ± 1.82 ms (mean ± SEM), n=21) (Figures 2D, and 2E). As an additional criterion, we measured the adapting properties of the thalamic units in response to repetitive, periodic whisker stimuli (Ahissar et al. 2000; Masri et al. 2008; Sitnikova and Raevskii 2010). Previous studies have shown that neurons in POm exhibit dramatic adaptation to persistent sensory stimulation, and a significant shift in response latency with the adaptation, as compared to VPm neurons. An example thalamic unit spiking response to an 8 Hz adapting whisker stimulus is shown on the left in Figure 2D, with a PSTH in response to the full stimulus train (top) and a superposition of the stimulus evoked response to the 1st (blue) and 8th (gray) deflection in the train (bottom). This particular example shows moderate adaptation (i.e. reduction in response amplitude), with a relatively small increase in latency of spiking. In fact, all the thalamic units that we considered for further analysis showed only moderate spike frequency adaptation (data not shown), with a maximal increased in latency of less than 20 ms comparing responses to the first and last stimulus of the train (Figure 2D Right and Supplementary Figure 1C (https://doi.org/10.6084/m9.figshare.13075940.v1), mean first spike latency (FSL), latency shift from Not-Adapted to Adapted = 4.28 ms ± 2.32 ms, mean ± SEM, n=21 cells from rat; 1.03 ms ± 1.24 ms, mean ± SEM, n=5 cells from mouse. Note that there remains a small possibility that a subset of the thalamic units is POm in origin, and project to S1 interbarrel areas (septa). However, this is unlikely to be the case for the thalamocortical pairs that showed monosynaptic connectivity, given that these thalamic and cortical units demonstrated single whisker receptive fields (Furuta et al. 2009) and the likelihood of detecting synaptic connections in PoM-S1 inter-barrel areas is much lower. Again, note that the challenges here are somewhat specific to this particular brain region, but achieving definitive recordings in other brain regions would likely have similar challenges to those described here.

Previous studies have shown that the convergence of thalamic inputs onto topographically aligned cortical layer 4 neurons is generally relatively high, but with the probability of contacting regular spiking units (RSUs) much lower than fast spiking units (FSUs) (Bruno and Simons 2002; Swadlow 2003). Here, we focused exclusively on fast spiking cortical units (FSUs), identified through their waveform shape (mean time from trough to peak: 0.3 ± 0.1 ms, n=21, see Methods). We recorded from well-isolated cortical

633 layer 4 neurons (unit quality 3.9 ± 1.9, n=21, defined as mean peak-to-peak voltage
634 divided by two standard deviation of waveform amplitude, see Methods) at a cortical
635 depth taken from micromanipulator readings (Rat: 803.28 ± 175.28 um, n=21, data not
636 shown). We found that the relative latency difference between VPm and S1 layer 4 in
637 aligned regions was comparable to the expected synaptic delay between VPm and S1
638 layer 4 (Figure 2E and Supplementary Figure 1D -
639 https://doi.org/10.6084/m9.figshare.13075940.v1, (rat): 11.25 ms ± 1.83 ms, mean ± SEM,
640 n= 21; (mouse): 10.48 ms ± 1.91 ms, n= 5 , differences between VPm-S1 were ~3 ms for
641 rat and ~1.3 ms for mouse). An example of the response to a punctate whisker stimulus
642 for a pair of VPm and S1 FS units with mean first-spike latency of 7.5 ms and 11.2 ms is
643 shown on the left of Figure 2E.
644
645 **Inferring connectivity in the context of a signal detection framework**
646 In general, neurons in the central nervous system require the concerted action of a
647 relatively large number of pre-synaptic inputs to produce an action potential (Bruno and
648 Sakmann 2006). Thus, the relationship between pre- and post-synaptic neurons is
649 tenuous at best, reflected in often a very subtle increase in the probability of firing of the
650 post-synaptic neuron a few milliseconds after the firing of a pre-synaptic neuron. The
651 analysis of spike trains from a pair of neurons can thus be utilized for a simple binary
652 classification of a neuronal pair either being 'not connected' or 'connected' (Figure 3A).
653 In order to infer connectivity, for each recorded pair of neurons, the raw spike cross-
654 correlogram is calculated using standard approaches (C_r, Figure 3C) (see Methods),
655 effectively yielding a histogram of cortical firing relative to thalamic spike times. Because
656 the analysis is based on spiking activity, and the baseline spiking activity can often be
657 relatively low, we drove the thalamocortical circuit in-vivo with a weak whisker stimulus
658 (Figure 3B, sinusoidal deflection, 4 Hz, mean velocity: 25 °/s), which is known to enhance
659 firing rates with minimal impact on firing synchrony across neurons (Bruno and Sakmann
660 2006). To correct for correlated stimulus-locked activity, we generated a shuffle-corrected
661 spike cross-correlogram (C_{sc}, Figure 3E) by subtracting the trial shuffled spike cross-
662 correlogram (C_s, Figure 3D) from the raw spike cross-correlogram. The "shuffled cross-
663 correlogram" is generated using the same procedure used for the raw cross-correlogram,
664 except that the trials of the thalamic and cortical spiking activity are randomized relative
665 to each other. This effectively destroys any elements of the cross-correlogram that are
666 not due to the stimulus. Shown in this example is the qualitative signature of
667 monosynaptic connectivity – a prominent peak in the shuffle-corrected cross-correlogram
668 for small positive lags that would be consistent with a single synaptic delay.
669
670 Then, to conclude that a neuronal pair was 'connected', we adopted two criteria that
671 expanded from previous studies (Bruno and Sakmann 2006; Reid and Alonso 1995;

672 Swadlow and Gusev 2001) based on both the raw and shuffle-corrected cross-
673 correlogram: (Criterion 1) a notable sharp, millisecond-fine peak is observed within a
674 narrow lag of 1-4 ms after a thalamic spike, that is the maximum in the raw cross-
675 correlogram; and (Criterion 2) this fast 'monosynaptic peak' is significant or still present
676 after accounting for (subtracting) stimulus-induced correlation. For the example
677 'connected' pair in Figures 3C-E and a separate 'not connected' pair, Criterion 1 is
678 evaluated from the raw cross-correlation as shown in Figure 4A, The raw cross-
679 correlogram on the right exhibits a peak within the central 1-4 ms lag (shown as a vertical
680 gray band), and thus passes Criterion 1, while the raw cross-correlogram on the left
681 exhibits a peak outside the central 1-4 ms lag, and thus fails Criterion 1. Figure 4B
682 illustrates how Criterion 2 is estimated from the shuffle-corrected cross-correlation. We
683 evaluate the prominence of the peak relative to a 99% confidence interval generated from
684 3.5 standard deviations of a distribution of peak magnitudes from shuffled cross-
685 correlograms, plotted in Figure 4B as the dashed lines. This is shown in more detail for
686 this example in the inset of Figure 4B, where the central portions of the shuffle-corrected
687 cross-correlograms are shown for each case. We define the metric related to Criterion 2
688 as the peak height, h, defined as the maximum of the C_{sc} (0.5 ms bin size) for 1-4 ms
689 lags, normalized by the standard deviation of the shuffled cross-correlogram. This metric
690 is thus the number of standard deviations the peak of the shuffle-corrected cross-
691 correlogram within the 1-4ms lag is above the shuffled distribution. Note that for the "not
692 connected" pair shown in Figure 4A and B, the shuffle-corrected cross-correlogram also
693 revealed the presence of the global peak outside the 1-4 ms central lag, similar to that of
694 the raw cross-correlogram. Thus, it is possible to utilize the shuffle-corrected cross-
695 correlogram for the evaluation of Criterion 1 in some cases, but overall, we found that
696 Criterion 1 was more robustly evaluated utilizing the raw cross-correlogram.
697
698 Note that to be classified as connected, a candidate pair of neurons must pass both
699 Criterion 1 and Criterion 2. Using these metrics and criteria, we can consider the result
700 of cross-correlation analysis for each pair as an inference problem in the context of a
701 signal detection framework, where we conceptualize the distribution of metric values for
702 the non-connected pairs as "noise", and for the connected pairs, as "signal". Applying the
703 criteria on the metric values yields four possible outcomes: Hit (connected pair
704 classified/inferred as such), Miss (connected pair classified/inferred as 'not connected'),
705 False Alarm (not-connected pair classified/inferred as 'connected'), and Correct Reject
706 (not-connected pair classified/inferred as such) (Figure 4C). With these metrics and
707 criteria, we classified measured neuronal pairs into 'connected' and 'not-connected'
708 distributions, with 6/22 pairs having a putative monosynaptic connection and 16/22 pairs
709 having no apparent connection (Figure 4C right, Rat: n =22 pairs & Supplementary Figure
710 1 for mouse data - https://doi.org/10.6084/m9.figshare.13075940.v1). For Criterion 1, this

711 was a binary classification – pairs having peak locations from their raw cross-
712 correlograms within the 1-4ms lag pass Criterion 1, and those which do not, fail Criterion
713 1. For Criterion 2, the dashed vertical line represents the 3.5 SD for the peak height metric
714 – pairs having peak height above this criterion line pass Criterion 2. Putting it altogether,
715 only pairs that passed both Criterion 1 and 2 in Figure 4C (right) were classified as
716 'connected' (anything to the right of vertical dashed line and on the top row) and the rest
717 were classified as 'not connected'. Note that while this is a binary classification, and the
718 end-result is a labeling of a pair as 'connected' or 'not-connected', not all classifications
719 are equivalent, with some having substantially more confidence in the classification than
720 others. By utilizing a bootstrapping approach (see Methods) and evaluating the likelihood
721 of specific outcomes using the pre-defined metrics and criteria for each recorded pair, we
722 were able to attach a probability measure (Figure 4C right, color bar) along with each
723 connectivity inference. In Figure 4C right, some of the cases that passed Criterion 1 have
724 peak heights that are substantially far away from the line for Criterion 2. As expected, the
725 likelihood of inferring monosynaptic connection for these cases was higher (~0.6-1) and
726 thus we have more confidence in the assertion, as compared to cases that are very close
727 to the criterion line for Criterion 2, or failed Criterion 1.
728
729 **Data-length effect on monosynaptic connection inference**
730 Inference of monosynaptic connectivity using cross-correlation analysis on extracellular
731 signals is highly dependent on the amount of collected data. Based on existing literature,
732 the recommended numbers of spikes were highly variable, ranging from 2000 to 10000
733 spikes (Swadlow and Gusev 2001; Wang et al. 2010), but were presented more as a
734 "rule-of-thumb" than based on systematic evaluation. Here, we systematically evaluated
735 data-length dependence effects on the connectivity inference outcomes. More specifically,
736 we measured the data-length effect by performing bootstrapping on the full dataset by
737 randomly selecting segments of data of increasing duration, as illustrated in Figure 5A.
738 Note that for this analysis, the effects of data-length were evaluated in the context of
739 Criterion 2, as this is the measure more prominently affected by data-length. In general,
740 the analysis is primarily sensitive to the number of spikes used in the estimates, rather
741 than the time duration of experimental data collection, and is sensitive to the number of
742 both VPm and S1 spikes (i.e. sufficient spiking from both is requisite). For this reason, we
743 utilized the geometric mean of the number of VPm and S1 spikes, calculated as the
744 square root of the product of the number of VPm and S1 spikes. Because we did not have
745 access to an established "ground truth" of a pair being either connected or not connected,
746 we utilized example pairs in which the analysis revealed a very clear classification, which
747 we subsequently utilized as ground truth for the analysis.
748

Shown are the results from such an analysis for a ‘not connected’ pair (Figure 5B-E) and a ‘connected’ pair (Figure 5F-I). We found that, when a functional connection was obviously not present, the correlated firing activity between a pair of neurons was indistinguishable from that expected from stimulus-induced correlation, reflected in the metric remaining well below the criterion line (3.5 SD) for all values of data-length, while however steadily increasing as a function of the geometric mean (also accompanied by a decrease in the variability of the metric as reflected in the SEM) (Figure 5C). Figure 5D shows the distributions of the estimated connectivity metric h for two particular data-lengths (geometric means of 1837 spikes and 4730 spikes), relative to the criterion line. Both of these distributions are clearly to the left of the criterion line, corresponding to high correct reject and low false alarm rates, relatively unaffected by data-length (Figure 5E).

In contrast, when a functional connection was apparent, limited data confounded the inference of ‘connected’ as the metric remained below the criterion line for smaller data-lengths (Figure 5G). For two particular data-lengths (geometric means of 3760 and 10201 spikes), the distributions of the estimated connectivity metric h are shown in Figure 5H, relative to the criterion line. While the longer data-length resulted in a distribution of the peak height that was clearly above the criterion line (easily passing Criterion 2), the shorter data-length resulted in a distribution whose mean was above the criterion line (barely passing Criterion 2), but with a substantial portion of the distribution below the criterion line, resulting in a hit rate of 87.7% and miss rate of 12.3%. We found that the data-length required to reach a consistently correct inference was approximately 5000 spikes for this example (Figure 5I).

From the results in Figures 5B-E and 5F-I, it appears that data-length was critical only for correctly identifying a connected pair, and did not directly affect the inference related to a “not connected” pair – in other words, the analysis is prone to type II errors as opposed to type I, and the type II error is strongly dependent upon data-length. It is important to point out that the data-length needed for sufficiently reducing the probability of error in the inference in Figure 5I is dependent upon the ground truth value for the connectivity metric h, as well as the variance in the estimator. We thus analyzed the estimator bias and variance across six ‘connected’ pairs, as a function of the data-length, which we could systematically vary by utilizing sub-sampling of the full datasets. Figure 5J shows the bias in the estimator for the connectivity metric h, as a function of the geometric mean number of spikes, with generally a negative bias (an underestimate) and a clear exponential decrease in bias with data-length as expected, as the full data-length is approached. Figure 5K shows the corresponding variance in the estimator of the connectivity metric h, again as a function of the geometric mean number of spikes. Although some of the measures exhibited an apparent invariance to the data-length, overall, this quantity

788 decreased exponentially with increasing geometric mean number of spikes, again as
789 expected. For the set of 'connected' pairs of thalamic and cortical neurons here, the
790 geometric mean number of spikes required for the lower bound of resampled data to pass
791 Criterion 2 is shown in Figure 5L, with a median of approximately 9000 spikes.
792
793 **Thalamic synchrony effects on monosynaptic connection inference**
794 Without having access to the subthreshold activity of the postsynaptic cortical neurons,
795 assessment of connectivity through the co-occurrences of spiking activity in thalamic and
796 cortical neurons often necessitates activation of the intact circuitry with exogenous
797 stimulation due to relatively low intrinsic spontaneous firing rates. The analysis of Figure
798 5 revealed a clear motivation for acquiring larger numbers of spikes, which can obviously
799 be facilitated through increased mean firing rates. In sensory pathways, previous studies
800 have used sensory stimuli of varying strengths to evoke higher firing rate in primary
801 sensory areas (Bruno and Sakmann 2006; Reid and Alonso 1995; Sedigh-Sarvestani et
802 al. 2017; Wang et al. 2010), citing a rule-of-thumb which involves increasing the number
803 of spikes through external stimulation, but not with a stimulus so strong as to induce
804 stimulus-driven synchronization in spiking. Although this approach is logical, it remains
805 ad hoc, and the exact ramifications are not clear. Here, we utilized silicon multi-electrode
806 probes in the thalamic VPm and S1 layer 4 to quantify changes in neural activity across
807 spontaneous and stimulus driven conditions, and performed analyses to systematically
808 evaluate the potential effects of stimulus-driven changes in firing rate and synchrony on
809 the monosynaptic connection inference between VPm and S1 pairs. Figure 6A shows
810 simultaneous recordings from two thalamic neurons (VPm1 and VPm2) within the same
811 thalamic barreloid and a single cortical S1 neuron in the homologous barrel column. For
812 this example, VPm1 and S1 were revealed to be 'connected', while VPm2 and S1 were
813 clearly 'not connected'. Under increasingly stronger stimulus drive, from spontaneous
814 (left), to weak-sinusoidal whisker stimulus drive (middle), and to strong repetitive,
815 punctate whisker stimulus drive (right), there is a general increase in firing rate across the
816 recorded cells in both VPm and S1 (Figure 6B). In addition to the modulation of mean
817 firing rate, we found that increasing stimulus drive affected the inference of connectivity
818 by producing inconsistent conclusions across stimulus conditions, especially obvious with
819 increasingly strong stimuli. Interestingly, we found that this preferentially affected the
820 location of the peak in the cross-correlogram, which is associated with Criterion 1
821 evaluated through the raw cross-correlogram. Figure 6C shows the raw spike cross-
822 correlograms for each pair, across the stimulus conditions, where the top panel shows
823 this for the connected pair VPm1-S1, and the bottom panel shows this for the not-
824 connected pair VPm2-S1. Note that we were able to maintain stable recordings for this
825 particular group of neurons over a relatively long experimental time period, enabling us
826 to collect a sufficient number of spikes in the spontaneous condition in order to make

827 inferences regarding connectivity, which we can treat as ground truth here (VPm1-S1
828 connected, VPm2-S1 not-connected). First considering the connected pair VPm1-S1 (top
829 row), we found that the correct inference remained consistent ('connected') for
830 spontaneous (I) and sinusoidal (II) stimulus conditions as it passed both Criterion 1 and
831 2. However, for the repetitive transient (III) stimulus condition (bottom row), while the peak
832 height in the shuffle-corrected cross-correlogram exceeded the criterion line (thus
833 satisfying Criterion 2, not shown), there was a disappearance of an isolated peak in the
834 1-4 ms lag of the raw cross-correlogram, which is a violation of Criterion 1. This led to the
835 incorrect inference of 'not connected' for the case of the strong, transient stimulus, or a
836 "miss" in the language of signal detection theory. From our recorded datasets, we found
837 that distinct sets of 'connected' pairs were inferred in twelve simultaneously recorded
838 thalamocortical pairs across all stimulus conditions. Importantly, the pairs that were
839 inferred to be connected under weak stimulus condition (spontaneous and sinusoidal)
840 were entirely different from those inferred to be connected from the strong stimulus
841 condition (transient) (data not shown).
842
843 Turning to the 'not-connected' pair VPm2-S1 in the bottom row of Figure 6C, note that for
844 the spontaneous (I) and sinusoidal (II) case, while the peak height of the shuffle-corrected
845 cross-correlogram exceeded 3.5 SD (thus passing Criterion 2, not shown), we correctly
846 inferred 'not connected' for these stimulus conditions given the violation of Criterion 1.
847 Surprisingly, we incorrectly inferred 'connected' for the repetitive transient (III) stimulus
848 condition as fast peaks emerged in the 1-4 ms lag of the raw cross-correlograms,
849 satisfying Criterion 1 (and also Criterion 2, not shown), or a "false alarm" in the language
850 of signal detection theory. We thus encountered two kinds of errors when utilizing
851 exogeneous stimulation to increase neuronal firing rates – "misses" and "false alarms",
852 both linked to Criterion 1, due to appearance of spurious peaks in 1-4 ms lag in the cross-
853 correlogram.
854
855 In previous studies, increase in stimulus-driven firing rate has been shown to couple with
856 higher degree of synchronization within and across neural circuits (Temereanca et al.
857 2008; Wang et al. 2010) that can potentially dominate the temporal relationship of the
858 network dynamics revealed by correlational analysis (Ginzburg and Sompolinsky 1994).
859 This highlights the issues underlying the tradeoff between firing rate and synchronization
860 of the local network that are intrinsic to the correlational analysis used for monosynaptic
861 connection inference. Several paired recording studies have approached this problem by
862 collecting spontaneous spiking data (Swadlow and Gusev 2001), where presumably the
863 spontaneous activity is less synchronous than stimulus driven activity, or by providing
864 weak or non-synchronizing inputs to probe the circuit (Bruno and Sakmann 2006; Bruno
865 and Simons 2002; Reid and Alonso 1995). However, some degree of synchronization is

always present, and a direct understanding of the potential effects and implications of population synchronization of presynaptic neurons on monosynaptic connection inference is lacking. To relate the amount of synchronization across the thalamic units with the increase in stimulus strength, we quantified synchrony using the spike cross-correlogram measured across thalamic pairs. Specifically, the synchrony was defined as the number of spikes of the cross-correlogram within a window of +/- 7.5 ms, normalized by the number of thalamic spikes (see Methods). The raw spike cross-correlograms for the two VPm units shown in Figure 6A and 6C are shown in Figure 6E (top and orange symbol), illustrating an increase in the central peak of the cross-correlogram and thus the thalamic synchrony, note the emergence of sharp peaks from spontaneous to transient stimulus. Additionally, population data showed significant increases in thalamic synchrony comparing spontaneous and transient conditions, as well as sinusoidal and transient conditions (Figure 6D, n=10 pairs). To more generally quantify the relationship between thalamic synchrony and mean firing rates, across several experiments we collected thalamic responses to different stimuli (spontaneous, sinusoidal (25 deg/s) and transient stimuli of different velocities (50, 125, 300, 600, 900, and 1200 deg/s), producing a range of firing rates and corresponding degrees of synchrony, displayed in Figure 6E. In general, there was a monotonic increase in thalamic synchrony with firing rate, fit well by an exponential function (Figure 6E, blue curve).

To more systematically explore the relationship between the measured thalamic synchrony and Criterion 1 of the thalamocortical connectivity inference, we generated a set of simulations based on experimental data to demonstrate how increasing degrees of thalamic synchrony could influence the connectivity inference. Described in more detail below, the simulations were based on introducing spiking activity that corresponds to varying degrees of synchrony into the experimentally observed spiking activity at the levels of both thalamus and cortex. As described above for experimental observations, through these simulations we also found that the synchronization of the presynaptic thalamic population could potentially produce errors in two scenarios: misses (i.e. a connected pair being incorrectly inferred as “not connected”, denoted C →NC) and false alarms (i.e. a not connected pair being incorrectly inferred as ‘connected’, denoted NC → C).

We first sought to simulate the scenario of the top row of Figure 6C, where a pair of connected thalamocortical neurons (VPm1-S1) was misclassified as not-connected because a significant maximum peak was not detected in the central 1-4 ms lag of the raw cross-correlogram (violating Criterion 1, rightmost panel). We hypothesized that this experimental observation was due to a significant increase in cortical firing that was caused by inputs of nearby VPm neurons also connected to the same cortical neuron S1,

905 but relatively synchronous with the reference thalamic neuron VPm1. For this simulation,
906 we therefore emulated this scenario by reintroducing jittered spikes from VPm1 and S1
907 back into these datasets, respectively. Importantly, we found from our experimental
908 observations that the mean thalamic and cortical firing rate increased with stimulus
909 strength, but cortical firing increased to a lesser extent as compared to thalamic firing (not
910 shown). Therefore, the number of added spikes and the jitter (zero-mean Gaussian noise
911 of a specific standard deviation, σ) were both set to produce a specified level of synchrony
912 between the original and perturbed VPm1 spike train and also match the observed firing
913 rates in both VPm and S1 for this particular condition. The resultant thalamic and cortical
914 activity was denoted as VPm1* and S1*, respectively. With these manipulations, we
915 performed the analysis of connectivity as before between VPm1* and S1* at each firing
916 rate level (with corresponding thalamic synchrony level) to generate the probability of the
917 connectivity inference (i.e. probability of satisfying Criterion 1 reported as the fraction of
918 bootstrapped iterations results in satisfying Criterion 1). We found that the probability of
919 inferring a connection dropped with increasing thalamic synchrony as shown in the top of
920 Figure 6F, similar to what we observed in the actual experimental data (Figure 6C, top
921 right). For low levels of synchrony (e.g. thalamic synchrony measures of 0.2 or less), the
922 probability of satisfying Criterion 1 (and thus making the correct inference, given that
923 Criterion 2 is satisfied) remained relatively high (from ~0.6 to 0.9). However, increasing
924 levels of thalamic synchrony (and certainly above 0.5), the probability of satisfying
925 Criterion 1 approached 0 (and thus the chance of a miss neared 100%). The raw spike
926 cross-correlogram for two synchrony levels (highlighted with the green and blue vertical
927 dashed lines in Figure 6F top) are shown below the cross-correlogram, illustrating the
928 disappearance of the peak in the 1-4ms lag with increased synchrony. Note that for
929 artificially high levels of synchrony, approaching near perfect synchrony, the probability
930 of satisfying Criterion 1 does gradually come back up and approach the same probability
931 as for very low levels of synchrony, as expected (not shown for simplicity).
932
933 On the other hand, we found that in addition to causing the incorrect classification of a
934 connected pair (i.e. a “miss”), the thalamic synchrony induced by increased stimulus drive
935 could also have the opposite effect – the incorrect classification of a not-connected pair
936 as connected (i.e. a “false-alarm). When considering a thalamocortical pair that is not
937 synaptically connected (VPm2-S1), increased stimulus drive introduces the presence of
938 spiking in the S1 neuron induced by nearby VPm neurons that serve as synaptic inputs
939 to the S1 neuron in question. When these VPm neurons become increasingly
940 synchronous with VPm2, this results in the presence of a peak in the raw cross-
941 correlogram in the 1-4ms bin, satisfying Criterion 1 and thus resulting in a “false alarm”.
942

For a demonstration of this phenomenon, from experimentally obtained data, we conducted a simple simulation designed to systematically explore this effect. Specifically, in addition to the not-connected pair in question, VPm2-S1, we identified a distinct, simultaneously recorded thalamocortical pair that was inferred to be connected. By introducing spikes from the connected thalamic and cortical neuron into the spike trains of VPm2 and S1, respectively, the degree of thalamic synchrony was systematically increased as a function of the number of spikes added, but at the same time introduced the presence of cortical spiking from the connected pair. As with the first simulation, the number of spikes added to VPm2 and S1 was set to match the observed thalamic and cortical firing rates for this condition, to produce the perturbed spikes trains VPm2* and S1*. With these manipulations, we performed the analysis of connectivity as before between VPm2* and S1* at each firing level (with corresponding thalamic synchrony level) to generate the probability of the connectivity inference (i.e. probability of satisfying Criterion 1 reported as the fraction of bootstrapped iterations results in satisfying Criterion 1), as with the first simulation. We found that as thalamic firing became more similar with increasing amount of mixing (reflected in an increase in thalamic synchrony), the raw cross-correlogram exhibited the increased likelihood of a peak in the 1-4ms bin. Correspondingly, the probability of error rapidly increased with thalamic synchrony (probability of satisfying Criterion 1 exceeds 0.5 as thalamic synchrony reaches 1.5 in Figure 6G). The raw spike cross-correlogram for two synchrony levels (highlighted with the green and blue vertical dashed lines in Figure 6G top) are shown below the cross-correlogram, illustrating the appearance of the peak in the 1-4ms lag with increased synchrony. Although these simulations should be considered primarily in terms of the basic trends they exhibit, the rapid increase in the probability of error with thalamic synchrony suggests that above some level of synchrony in the pre-synaptic population, false-alarms are inevitable.

Probabilistic measure of connectivity inference across brain structures in large-scale recordings

Through the advent of high channel-count electrophysiological recording techniques (Chung et al. 2019; Jun et al. 2017; Rios et al. 2016), the diversity of recording quality, cell type, and possibilities for connectivity has expanded tremendously. To demonstrate how our framework can be beneficial, Figure 7 shows an example of simultaneous topographically aligned recordings from silicon multi-electrode probes inserted in VPm thalamus (Figure 7A) and S1 (Figure 7B). Specifically, focusing on portions of the probes that were assessed to be topographically aligned, a subset of channels from the VPm probe (Channels A-D) yielded 5 well-isolated single thalamic neurons (VPm 1-5), while a subset of channels from the S1 probe (A-D) yielded 4 well-isolated single cortical neurons

(S1 1-4). These neurons were recorded during weak sinusoidal (25 deg/s, 4Hz) whisker stimulation. In this multi-dimensional analysis, each of the 20 thalamocortical pairs were assessed for the possibility of connectivity. Table 1 in Figure 7C shows the matrix of binary outcomes of monosynaptic connectivity inference from cross-correlation analysis of the full dataset across the recording sites. Out of the 20 VPm-S1 pairs, 3 were judged to be connected according to our criteria. Note that while the connectivity from an individual barreloid to the homologous cortical barrel is relatively high (it has been estimated that approximately 1 in 3 VPm neurons within a barreloid is connected to a particular neuron in cortical layer 4 of the homologous barrel (Bruno and Sakmann 2006)), the relatively stringent criteria of the inference coupled with other factors such as the potential to record from multiple nearby VPm barreloids and variable single unit quality make this outcome typical. Shown in Figure 7C Table 2 are the probabilities of connectivity associated with each pair using the bootstrapping method (n = 1000 iterations) on the data (Table 2), as previously described. In general, the binary inference for a particular pair corresponded to the bootstrapped confidence levels – connected pairs had a relatively high probability of connectivity from the bootstrapping (see all 'connected' pairs in Supplementary Figure 2 - https://doi.org/10.6084/m9.figshare.13075943.v1), while not connected pairs had a relatively low probability of connectivity from the bootstrapping ($p<0.3$). However, there was a notable exception (VPm 4 – S1 1), where the associated probability is fairly low ($p=0.26$, see cross-correlograms in Supplementary Figure 2 - https://doi.org/10.6084/m9.figshare.13075943.v1). Not surprisingly, we found that the 'monosynaptic' peak in the cross-correlogram of this dataset was less prominent, almost indistinguishable from other spurious peaks that were outside of the 1-4 ms window. Previously, using a dataset with long recordings (>10 000 spikes), we showed that data-length could significantly affect peak height and cause misses in the inference. For this example, we found that the total number of spikes of this pair was about 3500 spikes (in terms of geometric mean), hence producing a low probability.

Discussion

The field of neuroscience is in a period of rapid tool development, spawned by a combination of innovative technologies and a shift in the focus of international scientific priorities. The explosion of tools for performing large scale neuronal recording at single cell resolution provides access to real-time monitoring of network activity within and across multiple brain regions (Ahrens et al. 2013; Chung et al. 2019; Jun et al. 2017). This access enables the exciting potential for interpretation of the causal flow of neuronal activity that ultimately underlies brain function, shaping of perception, and behavior (Sheikhattar et al. 2018). There have been significant efforts in anatomical tracing of connectivity and cell-type specific projections within and across brain regions and

hemispheres, leading to new insights into the detailed structure of brain circuits (Yuan et al. 2015). The ultimate goal is to understand how this complex structure gives rise to behaviorally relevant function through the dynamic interaction of neurons within the neural network. However, the identification of functional connections amidst perturbation-induced confounding variables in an intact brain remains very challenging despite increasing accessibility (Lepperød et al. 2018). Here, we provided an experimental and analytical framework for quantifying long-range synaptic connectivity that was developed and tested in the thalamocortical circuit of the rodent somatosensory pathway but is generalizable to other circuits and pathways. Importantly, we attacked this from a scalable statistical framework based on signal detection theory, where we established approaches to assess confidence in classification, and systematically examined factors contributing to the inference of connectivity.

The gold standard of studying and assessing synaptic connectivity involves direct manipulation of pre-synaptic neurons to observe a measurable postsynaptic effect. Hence, connectivity studies are often performed using in-vitro brain slices (Jiang et al. 2015; Pfeffer et al. 2013) due to better accessibility to pre- and postsynaptic neurons concurrently, which is difficult or intractable in-vivo (Jouhanneau et al. 2015; Jouhanneau et al. 2018; Pala and Petersen 2015). In attempts to identify connectivity in-vivo, previous studies have used electrical stimulation to conduct collision tests that involve comparing the timing of anti-dromic activation with stimulus evoked activity to verify origins of projection (Kathleen Kelly 2001; Swadlow 1989). Although this is a powerful and attractive approach, as it helps to more confidently assess connectivity and establish causal relationships, it does not scale well to assessing connectivity at the population level, where selective stimulation of individual neurons is not typically possible. As an alternative, we adopted non-synchronizing, weak sensory drive (Bruno and Sakmann 2006; Wang et al. 2010) to assess likely connectivity through spike cross-correlation analysis. Although this approach obviously does not address issues of causality directly, it scales with increasing size of population recordings in the pre- and post-synaptic regions, opening up the possibility for assessing connectivity using large, ensemble recordings (Juavinett et al. 2018).

The systematic evaluation of the parameters of analysis presented here offers the potential for the optimization of experiment design for the purpose of assessing connectivity. Although the details likely vary across brain region and experimental preparation, the results here do suggest some general rules of thumb, perhaps the most important of which revolve around the interplay between data-length and synchrony. For example, based on our data, we estimated that about ~9000 spikes (in terms of geometric means of total thalamic and cortical spikes) were needed to reach an inference with high

1058 certainty (95% confidence interval) in the fentanyl-anesthetized rat, consistent with
1059 recommended number of spikes used using similar stimulus conditions (Bruno and
1060 Simons 2002; Wang et al. 2010) and between 6800 and 10,000 spikes for spontaneous
1061 and sinusoidal conditions respectively in the isoflurane-anesthetized mouse (data not
1062 shown). Thus, the requirements were on the same order of magnitude for both of these
1063 cases, despite significant differences in experimental preparation (i.e. anesthesia, etc.)
1064 and differences in precise anatomical details across the species.
1065
1066 Synchrony across the pre-synaptic population has long been implicated as a potential
1067 confound in assessing synaptic connectivity, typically tied to false alarms (type 1 error),
1068 or the incorrect inference of connectivity in non-connected pairs (Ostojic et al. 2009). The
1069 results here supported this long-held assumption, where the artificially elevated
1070 synchrony in the VPm population resulted in the increased likelihood of satisfying
1071 Criterion 1, and importantly established ranges of measured synchrony for which this is
1072 more likely. Surprisingly, we also found that increased pre-synaptic synchrony could
1073 result in a different type of confound – a miss (type 2 error), or the incorrect inference of
1074 not-connected for connected pairs. Interestingly, this effect emerged over a relatively
1075 similar level of synchrony as determined through artificial elevation of the thalamic
1076 synchrony. As expected, spontaneous activity is typically fairly asynchronous, and in this
1077 regime, the types of errors described here are unlikely for this case. However, common
1078 drive through sensory input designed to elevate firing in otherwise sparse conditions
1079 increases the likelihood of these errors, and thus the tradeoff between increased data
1080 length and synchronization plays an important role in experimental design. This is further
1081 important in extending this approach to awake, behaving conditions, with increased firing
1082 rates, and continuous modulation in population synchrony by brain state.
1083
1084 Although the approach here was developed with generality in mind, there are several
1085 potential limitations related to the specific details of the experimental preparation. First,
1086 the data collected in this study were from immobilized, anesthetized rodents. This enabled
1087 relatively stable and long-duration recordings that are increasingly difficult in the awake,
1088 and moving, animal, where the data-length effects may preclude accurate identification
1089 of synaptic connectivity. Second, the thalamocortical circuit is built on anatomy that is
1090 well-studied, and highly convergent, with approximately 50-100 thalamic relay neurons
1091 making synapses onto a cortical layer 4 neuron with a clear topography (Bruno and
1092 Sakmann 2006). This convergent nature of the thalamocortical projections provides
1093 significant support in assessing possible connectivity, in contrast to potential connectivity
1094 across cortical laminae or other less topographically organized projections. Third, the
1095 VPm relay neurons are reported to be uniformly excitatory, thus the pre-synaptic spiking
1096 enhances the likelihood of action potentials in the post-synaptic cortical target. Although

long-range projections typically tend to be excitatory rather than inhibitory, analogous approaches should certainly be developed for inhibitory connectivity that is becoming increasingly acknowledged to play a complex and pivotal role in controlling network dynamics (Isaacson and Scanziani 2011).

With the scaling up of electrophysiological recordings comes challenges. In this work, we performed highly curated, small scale electrophysiological recordings to evaluate dynamics of VPm (potential pre-synaptic) and S1 (potential post-synaptic) neurons on a pair-by-pair basis as well as large-scale pre- and post-synaptic recordings, where any pair of neurons from the upstream and downstream structures would be a candidate for connectivity inference. What comes hand-in-hand with increasing recording yield that enables us to better answer questions about circuit function is an increasing diversity of recording quality, increasing diversity of cell type, and a wide array of possibilities for connectivity. In our hands, we found that the odds of finding putative monosynaptic connections per recording session increased by at least two- to three-fold. However, the nature of neural data collection is fundamentally changing, where large-scale recordings of populations of neurons are acquired without the continual fine tuning of electrode placement of the past decades. Previous studies suggest that high signal quality can be obtained with multi-site recording due to its better detectability of extracellular feature across closely spaced contacts (Buzsáki 2004; Gray et al. 1995; Harris et al. 2000). Yet, in practice, handling large amounts of data with probe recordings presents challenges as most of the spike sorting algorithms to-date require manual curation to improve spike classification. This suggest that a certain amount of contamination of spikes from neighboring cells is to be expected. Overall, large-scale recording of neuronal activity will reduce the number of animals, reveal important information only available from monitoring the interaction of brain networks, but the variability inherent in these datasets drives the need for a more comprehensive approach for diverse neuronal ensembles. Traditionally, cross-correlation analysis of homogeneous, highly curated, small scale electrophysiological recordings was primarily used to attach a binary outcome for concluding monosynaptic connection in-vivo (Bruno and Simons 2002; Fujisawa et al. 2008; Miller et al. 2001; Reid and Alonso 1995; Swadlow 2003; Swadlow and Gusev 2001) and data with uncertainties were often discarded. In this work, the evaluation of the neuronal data would not result in a binary classification of connected or not, but instead the assignment of a likelihood of connectivity based on the statistical framework we present here, producing a probabilistic connectivity map. While this approach was developed through analysis of extracellular neuronal spiking data, we also envision that this would be readily adapted to optical imaging approaches that enable cellular resolution calcium or voltage imaging of population spiking activity. Recently, model-based approaches to improve connectivity estimation are being developed for the analysis of

large datasets (Chen et al. 2011; Kobayashi and Kitano 2013; Kobayashi et al. 2019; Lütcke et al. 2013; Okatan et al. 2005; Paninski et al. 2004; Stevenson et al. 2008; Zaytsev et al. 2015). These methods typically involve fitting neuronal data or correlational relationships from recordings through models (i.e. generalized linear models (GLMs)) and further aim to reconstruct neuronal circuitry to estimate functional connectivity or to decode causal flow. The statistical approach we present here could eventually be combined with these more structured network modelling approaches to provide a more comprehensive framework for assessing and understanding causal interactions in the brain.

Figure captions

Figure 1: Experimental approach used to estimate monosynaptic connectivity between somatotopically - organized areas of the rodent somatosensory pathway. A. Simultaneous single-unit extracellular recordings were performed in the ventral posteromedial (VPm) nucleus of the thalamus and in layer IV of primary somatosensory cortex (S1) in anesthetized rodents. Recordings were targeted to topographically-aligned barreloids in VPm and barrel column in S1. Weak stimulation was applied to the whisker corresponding to the recorded barreloid/barrel column to elicit non-synchronous spiking. Putative monosynaptic connection between pairs of neurons were inferred using cross-correlation analysis. **B.** Experimental procedures used to establish paired recordings involve (1) Animal preparation includes surgeries. (2) S1 mapping, (3) identification of the whisker corresponding to the recorded barreloid, (4) targeting corresponding S1 barrel column and layer IV, (5) data collection for assessing monosynaptic connectivity by generating spikes via whisker stimulation, repeating step (3), (4) and (5) for recording additional pairs and (6) histology.

Figure 2: Targeting topographical alignment in vivo. A. S1 targeting: Location of S1 barrels was determined using intrinsic imaging (IOS). The three images on the top are images acquired in response to separate single punctate deflections of the Beta whisker, the C2 whisker, and the B2 whisker, respectively. A barrel template was compared to the optical image of the brain surface through the thinned skull and fitted based on the location of the centroid of barrels to provide guidance for electrode placement. **B.** (Left) VPm targeting: example mean LFP amplitude of evoked response (shown by downward deflection after stimulus onset) for four stimulated whiskers. Note the largest and fastest response to the A3 vibrissa, and the comparatively weak responses to the adjacent B2, B3, and C3 vibrissae, lending support for VPm localization. **C.** Histological slice showed electrode tracks marked with fluorescent dyes (see Method: Post-mortem histology) on coronal brain sections targeting VPm (bottom) and S1 layer IV (top). Example raw voltage traces from extracellular recordings performed simultaneously in VPm and S1 layer IV during sensory stimulation. Mean waveforms of isolated single units from each recording site were shown (shaded region indicate one standard deviation of spike amplitude).**D.** Example adapting response of a single thalamic unit, showing mean first-spike latency in response to first and last pulse of a 8Hz pulsatile, ongoing stimulus (1st pulse: 5.18 ms, last pulse: 10.7 ms). (Right) Population adapting response for thalamic units (n=22 neurons, N = 12 rats). Thick blue line showing mean first spike latency for first and last pulse of an 8Hz pulsatile, ongoing stimulus. All thalamic units that we recorded showed latency shift less than 20 ms (latency shift= 4.28 ± 2.32 ms, n = 22 neurons, N = 12 rats), suggested that they were thalamic VPm units. **E.** (Left) Example peri-stimulus time histogram (PSTH, 1 ms binsize) for a thalamic and cortical unit in the 30-ms window following punctate (600°/s) whisker stimulus (indicated by black arrow at t=0). We computed mean first spike latency (FSL), defined as average latency of first spike in 30 ms response window after stimulus presentation for each unit (VPm: 8.72 ms, S1: 11.2

ms). (Right) Population mean first spike latency for all simultaneously recorded thalamic and cortical units (VPm: 8.12 ms ±1.82, S1: 11.25 ±1.83 ms, n = 22 neurons, N = 12 rats). Thick purple line showed the mean first spike latency for each region.

Figure 3: Monosynaptic connectivity inference using cross-correlation analysis.
A. Inferring monosynaptic connectivity from extracellular recordings performed in topographically aligned thalamocortical regions in-vivo resulted in binary consequences. A pair of neurons can be putatively classified as 'connected' or 'not connected', as shown in schematic. **B**. Raster plots showing whisker evoked spiking response under low velocity sinusoidal stimulation (mean velocity: 25 deg/s) for a representative example from thalamus and cortex. **C**. All cross correlograms was computed using VPm spike train as a reference. Occurrences of cortical spikes were measured at various time lags (25 ms window before and after a thalamic spike, with 0.5 ms step size; see Method: Monosynaptic Connectivity). **D.** Stimulus-driven cross-correlograms were constructed between the original reference VPm spike trains and the trial-shuffled cortical spike trains. **E.** Shuffled-corrected cross-correlograms was generated from subtracting the mean of shuffled cross correlograms from the raw cross-correlograms. Dotted gray lines denoted 3.5 standard deviation of the shuffled distribution.

Figure 4: Evaluation of monosynaptic connection inference in the context of a signal detection framework.
A. In the context of signal detection framework, we defined two distinct metrics and criteria to classify neuronal pairs into 'connected' and 'not-connected' distribution. Showing here are representative example pairs from each condition. Note the qualitative difference in raw cross correlograms (C_R), one with broad and distributed spikes in cross-correlogram (left) and another with sharp peaks (right) in 1-4 ms time lags (shaded gray). The first metric is the maximum peak of the raw cross-correlogram (C_R), and Criterion 1 was fulfilled if the maximum peak of the raw cross-correlograms was within 1-4 ms lag. **B.** Second metric is the peak height within the window of interest (1-4 ms bin), measured as maximum peak value in shuffled-corrected cross-correlogram (C_{SC}), normalized to the number of standard deviations (# of SDs) with respect to the shuffled distribution. Criterion 2 was fulfilled if the peak exceeded 3.5 standard deviation of the shuffled distribution. **C.** Within this framework, four possible outcomes are possible. Hit: There is connection and experimenter say "Yes, connected". Miss: There is connection, experimenter say "No, not connected". False Alarm: No connection and experiment still say "Yes connected". Correct Rejection: No connection, experimenter say "No, not connected"). In this context, we found that 6/22 pairs have putative monosynaptic connection (denoted as solid circles), 16/22 pairs were not connected. (n = 22 neurons, N = 12 rats) Additionally, we performed bootstrapping on each dataset to compute the probability of inferring connectivity based on the two criteria, denoted as color bar on the right (bootstrap iteration = 100).

Figure 5: Data-length dependence effect on monosynaptic connection inference.
A. Data-length dependence effect on connectivity inference was evaluated using subsampling method. Data length was measured in terms of geometric spikes, which was

calculated by taking the multiplication of the square roots of total VPm and S1 spikes. Random subsampling of dataset was performed in the unit of trials with 1000 iterations for each condition. **B.** Representative example pair of neurons from 'not connected' distribution. **C**. Mean and standard deviation of peak height from cross-correlogram were computed for each subsample of 'not-connected' example. Blue line, short data-length condition (GM: 1837 spikes). Green, long data-length condition. **D**. Distribution of peak height after bootstrapping for two data-lengths labeled in part I, [Blue (GM): 1837 spikes; Green (GM): 4730 spikes]. **E**. Probability of reaching correct inference for this example, CR: Correct Reject; FA: false alarm. **F- I.** Similar to B-E but for 'connected' example [Blue (GM): 3760 spikes, hit rate: 87.7%, miss rate: 12.3%; Green (GM): 10201 spikes, hit and miss rate: 100%, 0%]. **J**. Bootstrap estimator of bias for each data length. Scatterplot of population data for connected pairs (n=6 pairs, N = 3 rats). Bold, exponential fit (R^2=0.76). **K.** Variance of peak height at each data-lengths for pairs shown in J. Bold, 1st order polynomial (R^2 =0.62%). **L.** Geometric mean for all connected pairs (Median: 8741 spikes, n = 6 pairs, N = 3 rats).

Figure 6: Thalamic synchrony effect on monosynaptic connection inference.
A. Raster plots from simultaneously recorded thalamic and cortical units under spontaneous (no stimulus), sinusoidal stimulus (mean velocity: 25 deg/s) and transient inputs (1200 deg/s). **B.** Mean firing rate of thalamus (VPm, blue) and cortex (S1, red) of neuronal pairs were quantified across all three stimulus conditions. VPm: spontaneous: 1.32 ± 1.6 Hz (n = 6 neurons, N = 2 mice), sinusoidal: 2.82 ± 3.05 Hz (n = 6 neurons, N = 2 mice), transient: 4.40 ± 1,60 Hz (n = 6 neurons, N = 2 mice); S1: spontaneous: 1.25 ± 0.85 Hz (n = 6 neurons, N = 1 mouse), sinusoidal: 2.97 ± 1.90 Hz (n = 4 neurons, N = 1 mouse), transient: 3.24 ± 1.2 Hz (n = 6 neurons, N = 1 mouse) (* indicating p< 0.5, Wilcoxon signed-rank test) **C.** Monosynaptic connectivity inference for two example thalamocortical pairs. [Checkmark symbols indicated that the pair was being classified as putatively connected; cross symbols indicated that the pair was being classified as not connected]. **D.** Thalamic synchrony, quantified as the central area under the raw cross correlograms of two thalamic units (± 7.5ms) across all three stimulus conditions. (* indicating p<0.05, Wilcoxon signed-rank test). Spontaneous: 0.24 ± 0.15; Sinusoidal: 0.24 ± 0.19; Transient: 0.62 ± 0.36, mean ± SEM (n = 5 neurons, 10 pairs, N = 1 mouse). **E**. (Top) Cross-correlograms from one example thalamic pair in spontaneous and transient stimulus conditions (I. Spontaneous, III. Transient). Time window (± 7.5ms) was shown as shaded blue box on cross-correlograms. (Bottom**)** The relationship between thalamic synchrony and mean firing rate of respective thalamic pairs were quantified across various stimulus conditions, including spontaneous, sinusoidal, transient stimuli with six different velocities (n = 5 neurons, 10 pairs, N = 1 mouse). Blue line showing exponential fit of the relationship. **F.** Simulation based on experimental data to systematically explore degree of thalamic synchrony with increasing firing rate on an example pair of putatively connected (PC) thalamocortical pair. Note that the probability of inferring connectivity dropped with increasing thalamic synchrony, suggesting potential misses. **G**. Simulation based on experimental data to systematically explore degree of thalamic synchrony with increasing firing rate on an example pair of not connected (NC) thalamocortical pair. Note

that the probability of inferring a connection increased with higher synchrony, suggesting higher probability of false alarms.

Figure 7: Connectivity matrix for topographically aligned, simultaneous multi-site recordings.

A. Thalamic (VPm) probe recording. Five whisker-responsive thalamic units were isolated from 32-channel silicon probe site labeled A-D. Mean waveform of single units were shown on the right (shaded region indicate one standard deviation of spike amplitude). (n = 5 neurons, N = 1 mouse,). **B.** Cortical (S1) probe recording. Four whisker-responsive units, putatively from layer IV barrel cortex were isolated from 32-channel silicon probe site labeled A-D. Mean waveform of single units were shown on the right (shaded region indicate one standard deviation of spike amplitude). n = 4 neurons, N = 1 mouse. Table 1 showed binary outcomes of monosynaptic connectivity inference based on Criterion 1 and 2 of cross-correlation analysis. Table 2 showed a connectivity matrix tabulating probability of inferring a putative monosynaptic connection using bootstrapping method for each thalamocortical pair in Table 1 (bootstrap iteration = 1000).

References:

Ahissar E, Sosnik R, and Haidarliu S. Transformation from temporal to rate coding in a somatosensory thalamocortical pathway. *Nature* 406: 302-306, 2000.

Ahrens MB, Orger MB, Robson DN, Li JM, and Keller PJ. Whole-brain functional imaging at cellular resolution using light-sheet microscopy. *Nature Methods* 10: 413-420, 2013.

Barthó P, Hirase H, Monconduit L, Zugaro M, Harris KD, and Buzsáki G. Characterization of Neocortical Principal Cells and Interneurons by Network Interactions and Extracellular Features. *Journal of neurophysiology* 92: 600-608, 2004.

Berényi A, Somogyvári Z, Nagy AJ, Roux L, Long JD, Fujisawa S, Stark E, Leonardo A, Harris TD, and Buzsáki G. Large-scale, high-density (up to 512 channels) recording of local circuits in behaving animals. *Journal of Neurophysiology* 111: 1132-1149, 2014.

Borden PY, Ortiz AD, Waiblinger C, Sederberg AJ, Morrissette AE, Forest CR, Jaeger D, and Stanley GB. Genetically expressed voltage sensor ArcLight for imaging large scale cortical activity in the anesthetized and awake mouse (erratum). *Neurophotonics* 4: 039801, 2017.

Bruno RM, and Sakmann B. Cortex is driven by weak but synchronously active thalamocortical synapses. *Science* 312: 1622-1627, 2006.

Bruno RM, and Simons DJ. Feedforward mechanisms of excitatory and inhibitory cortical receptive fields. *The Journal of neuroscience : the official journal of the Society for Neuroscience* 22: 10966-10975, 2002.

Buzsáki G. Large-scale recording of neuronal ensembles. *Nat Neurosci* 7: 446-451, 2004.

Buzsáki G, Stark E, Berényi A, Khodagholy D, Kipke DR, Yoon E, and Wise KD. Tools for probing local circuits: high-density silicon probes combined with optogenetics. *Neuron* 86: 92-105, 2015.

Castejon C, Barros-Zulaica N, and Nuñez A. Control of somatosensory cortical processing by thalamic posterior medial nucleus: a new role of thalamus in cortical Function. *PloS one* 11: e0148169, 2016.

Chen Z, Putrino DF, Ghosh S, Barbieri R, and Brown EN. Statistical Inference for Assessing Functional Connectivity of Neuronal Ensembles With Sparse Spiking Data. *IEEE Transactions on Neural Systems and Rehabilitation Engineering* 19: 121-135, 2011.

Chung JE, Joo HR, Fan JL, Liu DF, Barnett AH, Chen S, Geaghan-Breiner C, Karlsson MP, Karlsson M, Lee KY, Liang H, Magland JF, Pebbles JA, Tooker AC, Greengard LF, Tolosa VM, and Frank LM. High-Density, Long-Lasting, and Multi-region Electrophysiological Recordings Using Polymer Electrode Arrays. *Neuron* 101: 21-31.e25, 2019.

Constantinople CM, and Bruno RM. Deep Cortical Layers Are Activated Directly by Thalamus. *Science* 340: 1591-1594, 2013.

Csicsvari J, Hirase H, Czurko A, and Buzsáki G. Reliability and state dependence of pyramidal cell-interneuron synapses in the hippocampus: an ensemble approach in the behaving rat. *Neuron* 21: 179-189, 1998.

Diamond ME, Armstrong-James M, and Ebner FF. Somatic sensory responses in the rostral sector of the posterior group (POm) and in the ventral posterior medial nucleus (VPM) of the rat thalamus. *Journal of Comparative Neurology* 318: 462-476, 1992.

English DF, McKenzie S, Evans T, Kim K, Yoon E, and Buzsáki G. Pyramidal Cell-Interneuron Circuit Architecture and Dynamics in Hippocampal Networks. *Neuron* 96: 505-520.e507, 2017.

Fiáth R, Raducanu BC, Musa S, Andrei A, Lopez CM, van Hoof C, Ruther P, Aarts A, Horváth D, and Ulbert I. A silicon-based neural probe with densely-packed low-impedance titanium nitride

microelectrodes for ultrahigh-resolution in vivo recordings. *Biosensors and Bioelectronics* 106: 86-92, 2018.

Franklin K, and Paxinos G. *The mouse brain in stereotaxic coordinates, compact. The coronal plates and diagrams*. Amsterdam: Elsevier Academic Press, 2008.

Fujisawa S, Amarasingham A, Harrison MT, and Buzsaki G. Behavior-dependent short-term assembly dynamics in the medial prefrontal cortex. *Nat Neurosci* 11: 823-833, 2008.

Furuta T, Kaneko T, and Deschenes M. Septal neurons in barrel cortex derive their receptive field input from the lemniscal pathway. *The Journal of neuroscience : the official journal of the Society for Neuroscience* 29: 4089-4095, 2009.

Ginzburg II, and Sompolinsky H. Theory of correlations in stochastic neural networks. *Physical review E, Statistical physics, plasmas, fluids, and related interdisciplinary topics* 50: 3171-3191, 1994.

Gollnick CA, Millard DC, Ortiz AD, Bellamkonda RV, and Stanley GB. Response reliability observed with voltage-sensitive dye imaging of cortical layer 2/3: the probability of activation hypothesis. *Journal of neurophysiology* 115: 2456-2469, 2016.

Gray CM, Maldonado PE, Wilson M, and McNaughton B. Tetrodes markedly improve the reliability and yield of multiple single-unit isolation from multi-unit recordings in cat striate cortex. *Journal of neuroscience methods* 63: 43-54, 1995.

Harris KD, Henze DA, Csicsvari J, Hirase H, and Buzsáki G. Accuracy of tetrode spike separation as determined by simultaneous intracellular and extracellular measurements. *J Neurophysiol* 84: 401-414, 2000.

Isaacson JS, and Scanziani M. How inhibition shapes cortical activity. *Neuron* 72: 231-243, 2011.

Jiang X, Shen S, Cadwell CR, Berens P, Sinz F, Ecker AS, Patel S, and Tolias AS. Principles of connectivity among morphologically defined cell types in adult neocortex. *Science* 350: 2015.

Jouhanneau J-S, Kremkow J, Dorrn AL, and Poulet JFA. In Vivo Monosynaptic Excitatory Transmission between Layer 2 Cortical Pyramidal Neurons. *Cell Rep* 13: 2098-2106, 2015.

Jouhanneau J-S, Kremkow J, and Poulet JFA. Single synaptic inputs drive high-precision action potentials in parvalbumin expressing GABA-ergic cortical neurons in vivo. *Nature Communications* 9: 1540, 2018.

Jouhanneau J-S, and Poulet JFA. Multiple Two-Photon Targeted Whole-Cell Patch-Clamp Recordings From Monosynaptically Connected Neurons in vivo. *Frontiers in Synaptic Neuroscience* 11: 2019.

Juavinett AL, Bekheet G, and Churchland AK. Chronically-implanted Neuropixels probes enable high yield recordings in freely moving mice. *bioRxiv* 406074, 2018.

Jun JJ, Steinmetz NA, Siegle JH, Denman DJ, Bauza M, Barbarits B, Lee AK, Anastassiou CA, Andrei A, Aydın Ç, Barbic M, Blanche TJ, Bonin V, Couto J, Dutta B, Gratiy SL, Gutnisky DA, Häusser M, Karsh B, Ledochowitsch P, Lopez CM, Mitelut C, Musa S, Okun M, Pachitariu M, Putzeys J, Rich PD, Rossant C, Sun W-l, Svoboda K, Carandini M, Harris KD, Koch C, O'Keefe J, and Harris TD. Fully integrated silicon probes for high-density recording of neural activity. *Nature* 551: 232-236, 2017.

Kathleen Kelly GEC, Jed A. Hartings, Daniel J. Simons, M. Axonal conduction properties of antidromically identified neurons in rat barrel cortex. *Somatosensory & motor research* 18: 202-210, 2001.

Kobayashi R, and Kitano K. Impact of network topology on inference of synaptic connectivity from multi-neuronal spike data simulated by a large-scale cortical network model. *Journal of computational neuroscience* 35: 109-124, 2013.

Kobayashi R, Kurita S, Kurth A, Kitano K, Mizuseki K, Diesmann M, Richmond BJ, and Shinomoto S. Reconstructing neuronal circuitry from parallel spike trains. *Nature Communications* 10: 4468, 2019.

Kodandaramaiah SB, Flores FJ, Holst GL, Singer AC, Han X, Brown EN, Boyden ES, and Forest CR. Multi-neuron intracellular recording in vivo via interacting autopatching robots. *Elife* 7: e24656, 2018.

Landisman CE, and Connors BW. VPM and PoM nuclei of the rat somatosensory thalamus: intrinsic neuronal properties and corticothalamic feedback. *Cereb Cortex* 17: 2853-2865, 2007.

Lepperød ME, Stöber T, Hafting T, Fyhn M, and Kording KP. Inferring causal connectivity from pairwise recordings and optogenetics. *bioRxiv* 463760, 2018.

Lien AD, and Scanziani M. Cortical direction selectivity emerges at convergence of thalamic synapses. *Nature* 558: 80-86, 2018.

London M, Roth A, Beeren L, Häusser M, and Latham PE. Sensitivity to perturbations in vivo implies high noise and suggests rate coding in cortex. *Nature* 466: 123-127, 2010.

Lütcke H, Gerhard F, Zenke F, Gerstner W, and Helmchen F. Inference of neuronal network spike dynamics and topology from calcium imaging data. *Frontiers in Neural Circuits* 7: 2013.

Masri R, Bezdudnaya T, Trageser JC, and Keller A. Encoding of stimulus frequency and sensor motion in the posterior medial thalamic nucleus. *J Neurophysiol* 100: 681-689, 2008.

Matsumura M, Chen D-f, Sawaguchi T, Kubota K, and Fetz EE. Synaptic Interactions between Primate Precentral Cortex Neurons Revealed by Spike-Triggered Averaging of Intracellular Membrane Potentials <em>In Vivo</em&gt. *The Journal of Neuroscience* 16: 7757, 1996.

Millard DC, and Stanley GB. Anatomically based Bayesian decoding of the cortical response to intracortical microstimulation. In: *2013 6th International IEEE/EMBS Conference on Neural Engineering (NER)*2013, p. 1457-1460.

Miller LM, Escabi MA, Read HL, and Schreiner CE. Functional convergence of response properties in the auditory thalamocortical system. *Neuron* 32: 151-160, 2001.

Nowak L, and J B. Cross correlograms for neuronal spike trains. Different types of temporal correlation in neocortex, their origin and significance. 2000, p. 53-96.

Okatan M, Wilson MA, and Brown EN. Analyzing functional connectivity using a network likelihood model of ensemble neural spiking activity. *Neural computation* 17: 1927-1961, 2005.

Ostojic S, Brunel N, and Hakim V. How Connectivity, Background Activity, and Synaptic Properties Shape the Cross-Correlation between Spike Trains. *The Journal of Neuroscience* 29: 10234-10253, 2009.

Pala A, and Petersen CC. In vivo measurement of cell-type-specific synaptic connectivity and synaptic transmission in layer 2/3 mouse barrel cortex. *Neuron* 85: 68-75, 2015.

Paninski L, Pillow JW, and Simoncelli EP. Maximum likelihood estimation of a stochastic integrate-and-fire neural encoding model. *Neural computation* 16: 2533-2561, 2004.

Paxinos G, and Watson C. The rat brain in stereotaxic coordinates. *Qingchuan Zhuge translate* 32: 2007.

Perkel DH, Gerstein GL, and Moore GP. Neuronal spike trains and stochastic point processes. II. Simultaneous spike trains. *Biophysical journal* 7: 419-440, 1967.

Pfeffer CK, Xue M, He M, Huang ZJ, and Scanziani M. Inhibition of inhibition in visual cortex: the logic of connections between molecularly distinct interneurons. *Nat Neurosci* 16: 1068-1076, 2013.

Raducanu BC, Yazicioglu RF, Lopez CM, Ballini M, Putzeys J, Wang S, Andrei A, Welkenhuysen M, Helleputte Nv, Musa S, Puers R, Kloosterman F, Hoof Cv, and Mitra S. Time multiplexed active neural probe with 678 parallel recording sites. In: *2016 46th European Solid-State Device Research Conference (ESSDERC)*2016, p. 385-388.

Reid RC, and Alonso JM. Specificity of monosynaptic connections from thalamus to visual cortex. *Nature* 378: 281-284, 1995.

Rios G, Lubenov EV, Chi D, Roukes ML, and Siapas AG. Nanofabricated Neural Probes for Dense 3-D Recordings of Brain Activity. *Nano Letters* 16: 6857-6862, 2016.

Rossant C, Kadir SN, Goodman DFM, Schulman J, Hunter MLD, Saleem AB, Grosmark A, Belluscio M, Denfield GH, Ecker AS, Tolias AS, Solomon S, Buzsaki G, Carandini M, and Harris KD. Spike sorting for large, dense electrode arrays. *Nat Neurosci* 19: 634-641, 2016.

Sedigh-Sarvestani M, Vigeland L, Fernandez-Lamo I, Taylor MM, Palmer LA, and Contreras D. Intracellular, In Vivo, Dynamics of Thalamocortical Synapses in Visual Cortex. *The Journal of Neuroscience* 37: 5250, 2017.

Sheikhattar A, Miran S, Liu J, Fritz JB, Shamma SA, Kanold PO, and Babadi B. Extracting neuronal functional network dynamics via adaptive Granger causality analysis. *Proceedings of the National Academy of Sciences* 115: E3869, 2018.

Sitnikova EY, and Raevskii V. The lemniscal and paralemniscal pathways of the trigeminal system in rodents are integrated at the level of the somatosensory cortex. *Neuroscience and behavioral physiology* 40: 325-331, 2010.

Stevenson IH, Rebesco JM, Miller LE, and Körding KP. Inferring functional connections between neurons. *Curr Opin Neurobiol* 18: 582-588, 2008.

Stoy WA, Kolb I, Holst GL, Liew Y, Pala A, Yang B, Boyden ES, Stanley GB, and Forest CR. Robotic navigation to subcortical neural tissue for intracellular electrophysiology in vivo. *Journal of Neurophysiology* 118: 1141-1150, 2017.

Swadlow HA. Efferent neurons and suspected interneurons in S-1 vibrissa cortex of the awake rabbit: receptive fields and axonal properties. *Journal of Neurophysiology* 62: 288-308, 1989.

Swadlow HA. Fast-spike interneurons and feedforward inhibition in awake sensory neocortex. *Cerebral Cortex* 13: 25-32, 2003.

Swadlow HA, and Gusev AG. The impact of 'bursting' thalamic impulses at a neocortical synapse. *Nat Neurosci* 4: 402-408, 2001.

Temereanca S, Brown EN, and Simons DJ. Rapid changes in thalamic firing synchrony during repetitive whisker stimulation. *The Journal of neuroscience : the official journal of the Society for Neuroscience* 28: 11153-11164, 2008.

Wang Q, Webber RM, and Stanley GB. Thalamic synchrony and the adaptive gating of information flow to cortex. *Nat Neurosci* 13: 1534-1541, 2010.

Whitmire CJ, Millard DC, and Stanley GB. Thalamic state control of cortical paired-pulse dynamics. *J Neurophysiol* 117: 163-177, 2017.

Whitmire CJ, Waiblinger C, Schwarz C, and Stanley GB. Information Coding through Adaptive Gating of Synchronized Thalamic Bursting. *Cell Rep* 14: 795-807, 2016.

Yu J, and Ferster D. Functional Coupling from Simple to Complex Cells in the Visually Driven Cortical Circuit. *The Journal of Neuroscience* 33: 18855, 2013.

Yuan J, Gong H, Li A, Li X, Chen S, Zeng S, and Luo Q. Visible rodent brain-wide networks at single-neuron resolution. *Frontiers in Neuroanatomy* 9: 2015.

Zaytsev YV, Morrison A, and Deger M. Reconstruction of recurrent synaptic connectivity of thousands of neurons from simulated spiking activity. *Journal of computational neuroscience* 39: 77-103, 2015.

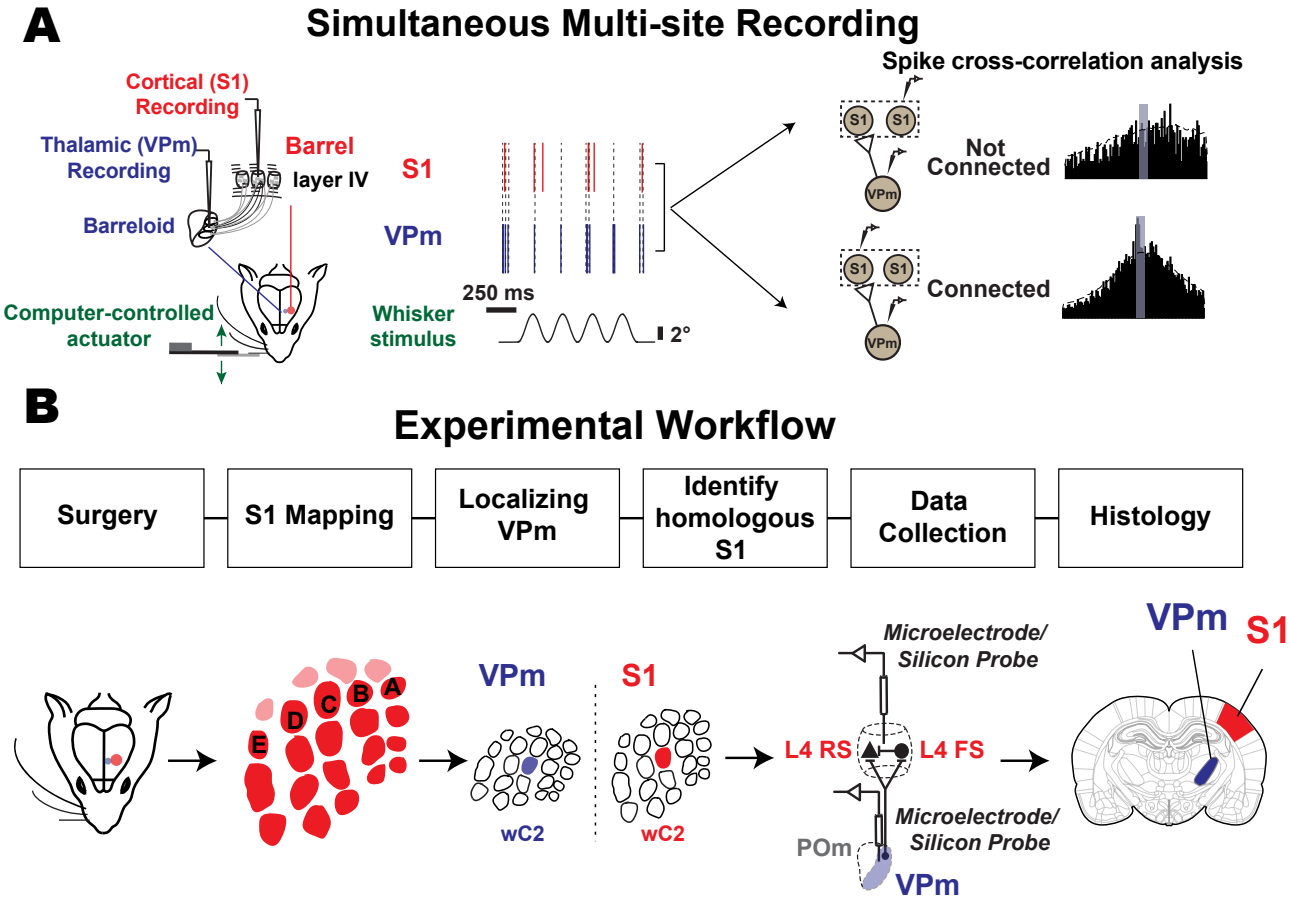
A
Simultaneous Multi-site Recording
Cortical (S1) Recording
Thalamic (VPm) Recording
Barrel
layer IV
Barreloid
Computer-controlled actuator
S1
VPm
250 ms
Whisker stimulus
2°
Spike cross-correlation analysis
S1
S1
VPm
Not Connected
Connected
B
Experimental Workflow
Surgery
S1 Mapping
Localizing VPm
Identify homologous S1
Data Collection
Histology
A
B
C
D
E
VPm
S1
wC2
wC2
Microelectrode/ Silicon Probe
L4 RS
L4 FS
POm
Microelectrode/ Silicon Probe
VPm
VPm
S1

Figure 1

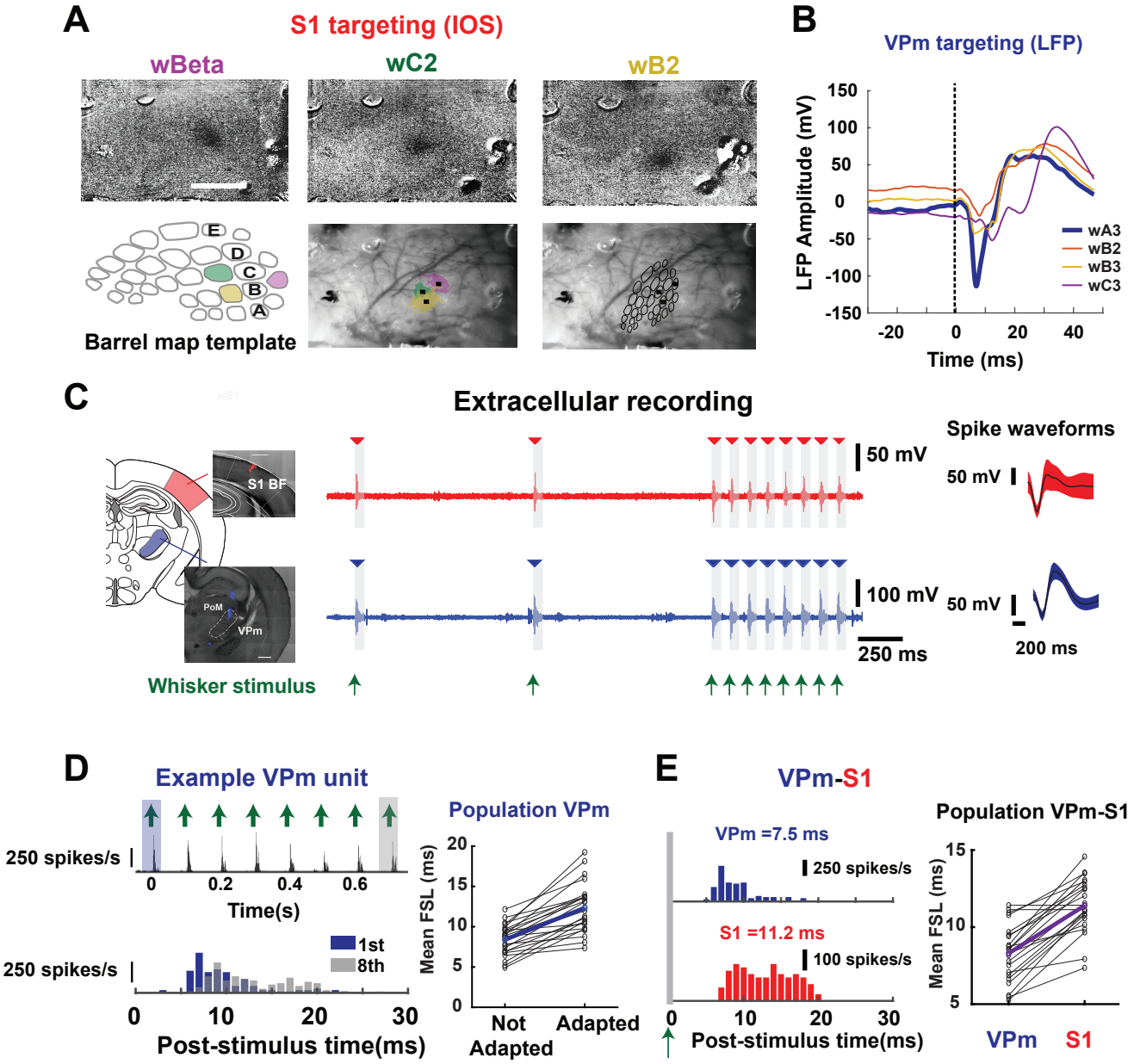
A
S1 targeting (IOS)
wBeta
wC2
wB2
E
D
C
B
A
Barrel map template
B
VPm targeting (LFP)
LFP Amplitude (mV)
150
100
50
0
-50
-100
-150
-20
0
20
40
Time (ms)
wA3
wB2
wB3
wC3
C
Extracellular recording
S1 BF
PoM
VPm
50 mV
100 mV
250 ms
Spike waveforms
50 mV
50 mV
200 ms
Whisker stimulus
D
Example VPm unit
250 spikes/s
0
0.2
0.4
0.6
Time(s)
250 spikes/s
1st
8th
0
10
20
30
Post-stimulus time(ms)
Population VPm
Mean FSL (ms)
20
15
10
5
0
Not Adapted
Adapted
E
VPm-S1
VPm =7.5 ms
250 spikes/s
S1 =11.2 ms
100 spikes/s
0
10
20
30
Post-stimulus time(ms)
Population VPm-S1
Mean FSL (ms)
15
10
5
VPm
S1

Figure 2

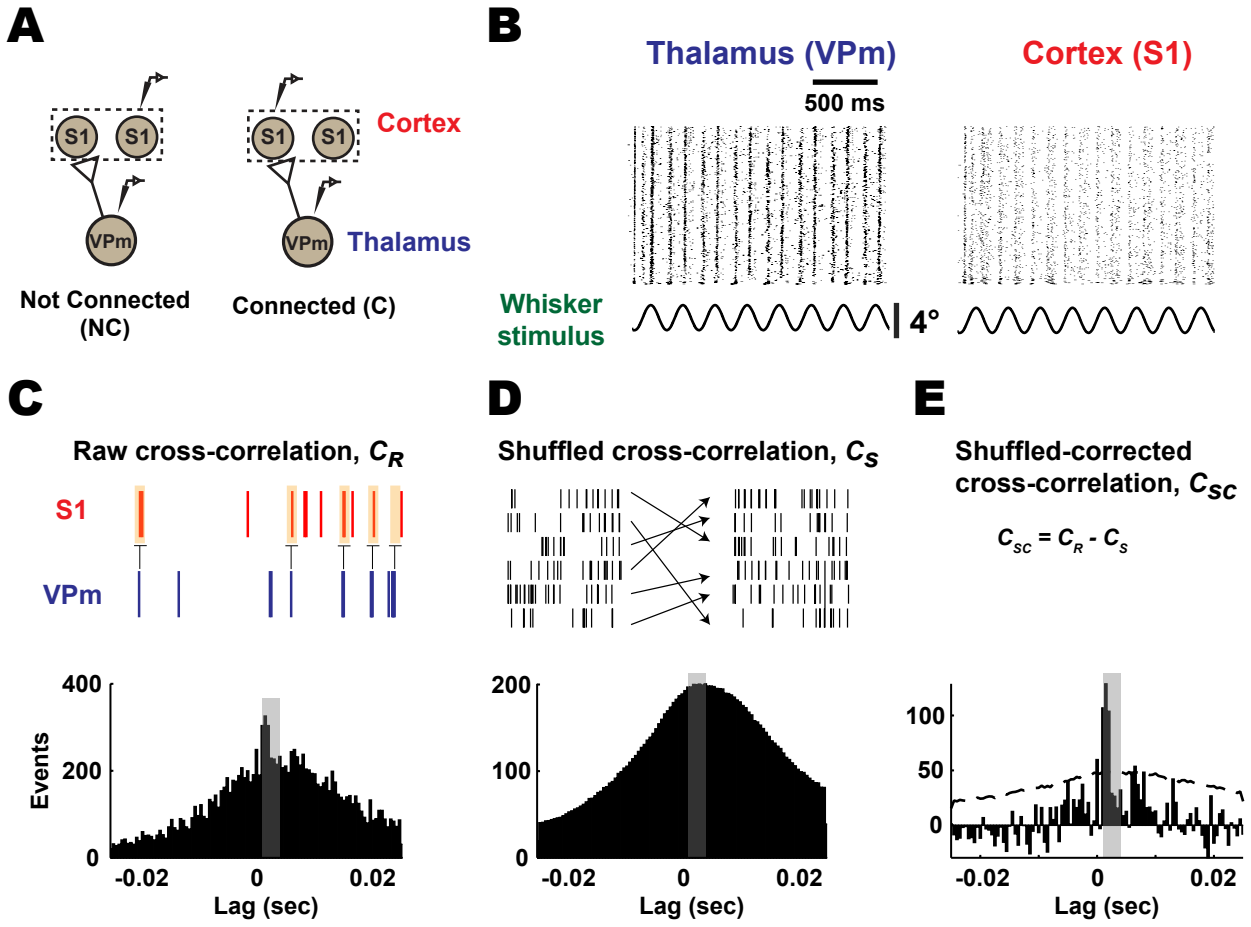
A
S1
S1
VPm
Not Connected (NC)
S1
S1
VPm
Cortex
Thalamus
Connected (C)
B
Thalamus (VPm)
Cortex (S1)
500 ms
Whisker stimulus
4°
C
Raw cross-correlation, C_R
S1
VPm
Events
400
200
0
-0.02
0
0.02
Lag (sec)
D
Shuffled cross-correlation, C_S
200
100
0
-0.02
0
0.02
Lag (sec)
E
Shuffled-corrected cross-correlation, C_{SC}
$C_{SC} = C_R - C_S$
100
50
0
-0.02
0
0.02
Lag (sec)

Figure 3

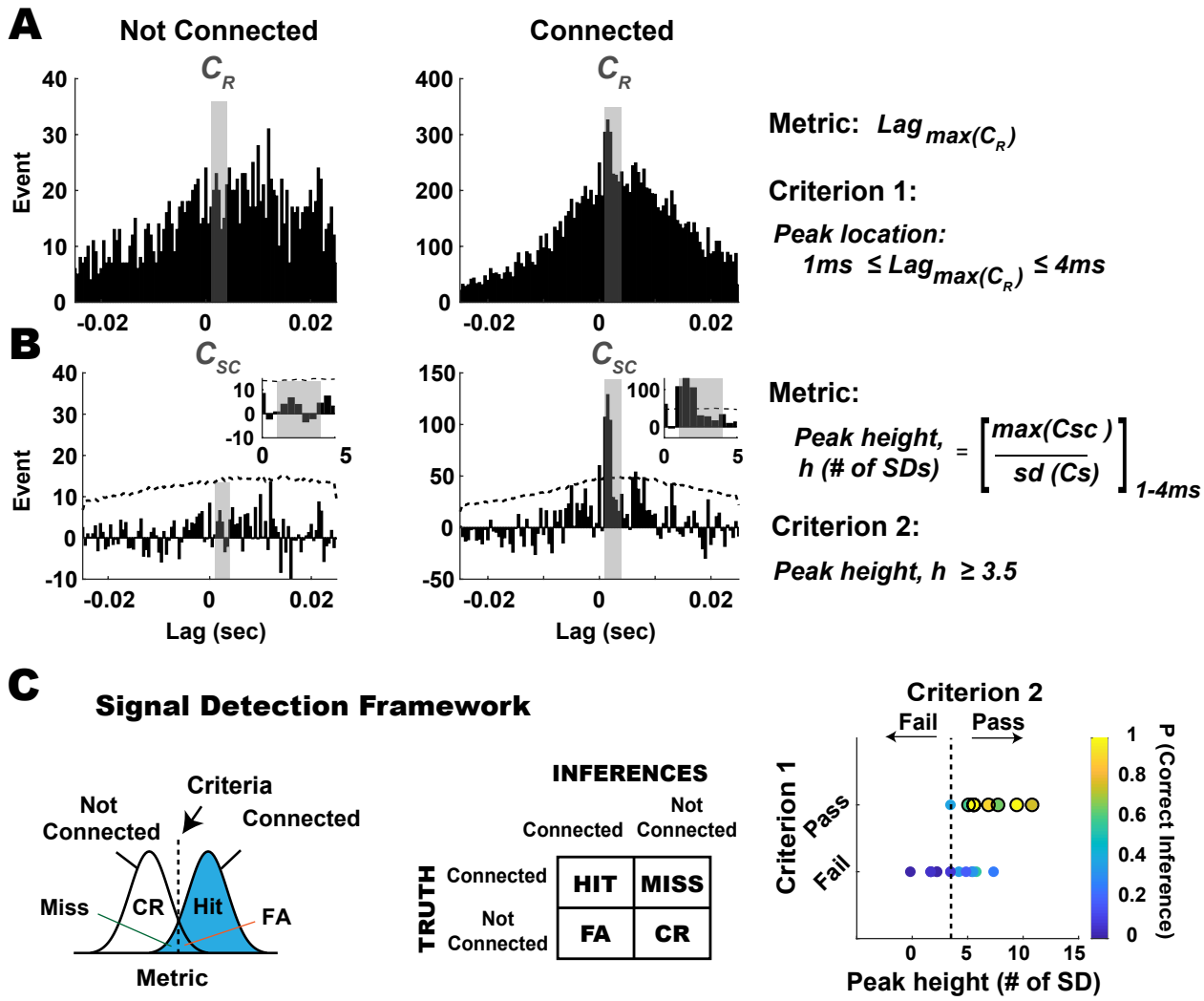
A
Not Connected
Connected
C_R
Event
Metric: $Lag_{max(C_R)}$
Criterion 1:
Peak location:
$1ms \leq Lag_{max(C_R)} \leq 4ms$
B
C_{SC}
Metric:
Peak height, h (# of SDs) = $\left[\frac{max(Csc)}{sd(Cs)}\right]_{1\text{-}4ms}$
Criterion 2:
Peak height, h ≥ 3.5
Lag (sec)
C
Signal Detection Framework
Criteria
Not Connected
Connected
Miss
CR
Hit
FA
Metric
INFERENCES
Connected
Not Connected
TRUTH
HIT
MISS
FA
CR
Criterion 2
Fail
Pass
Criterion 1
P (Correct Inference)
Peak height (# of SD)

Figure 4

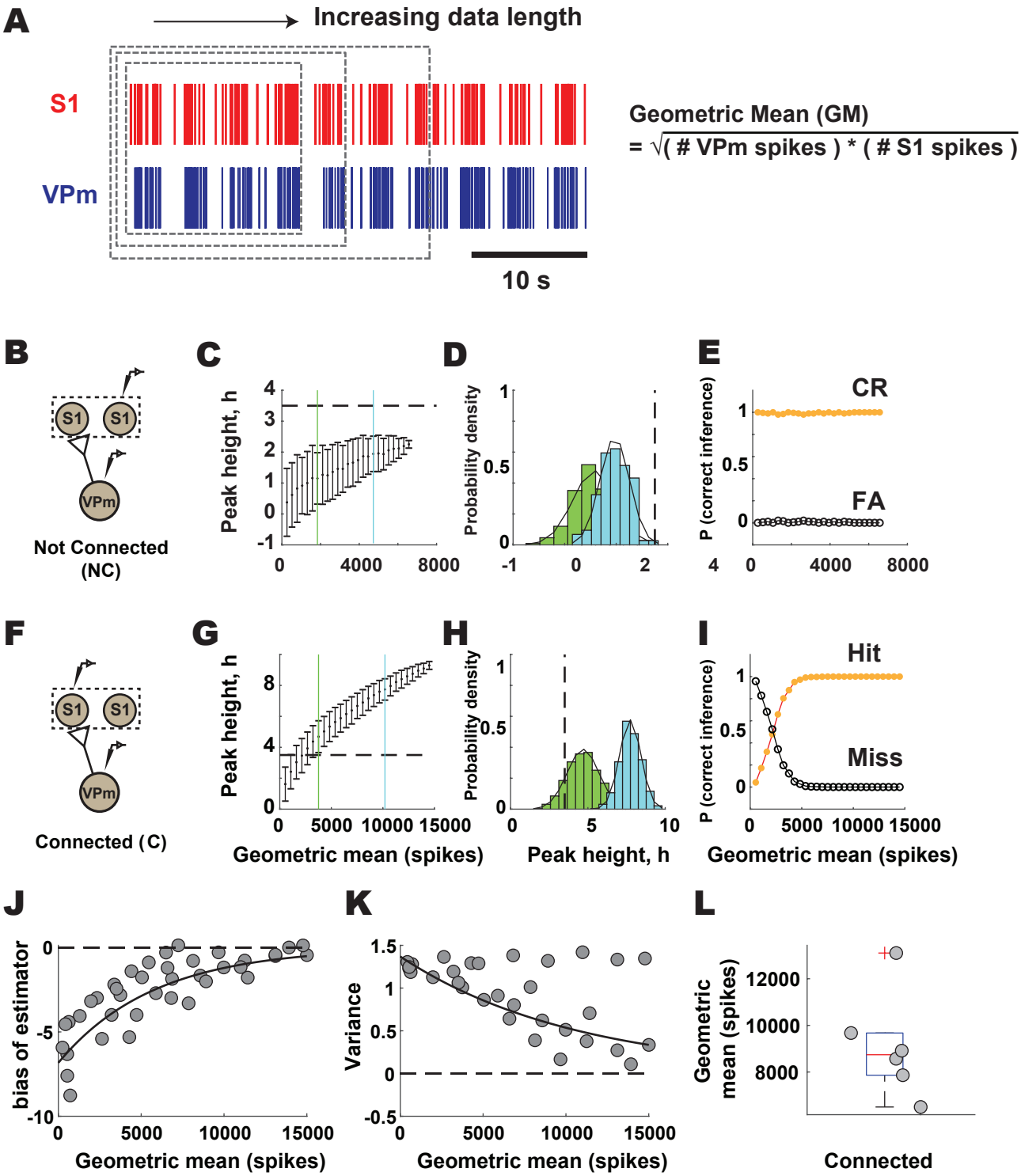
A
Increasing data length
S1
VPm
10 s
Geometric Mean (GM)
= √(# VPm spikes) * (# S1 spikes)
B
S1
S1
VPm
Not Connected
(NC)
C
Peak height, h
D
Probability density
E
CR
FA
P (correct inference)
F
S1
S1
VPm
Connected (C)
G
Peak height, h
Geometric mean (spikes)
H
Probability density
Peak height, h
I
Hit
Miss
P (correct inference)
Geometric mean (spikes)
J
bias of estimator
Geometric mean (spikes)
K
Variance
Geometric mean (spikes)
L
Geometric
mean (spikes)
Connected

Figure 5

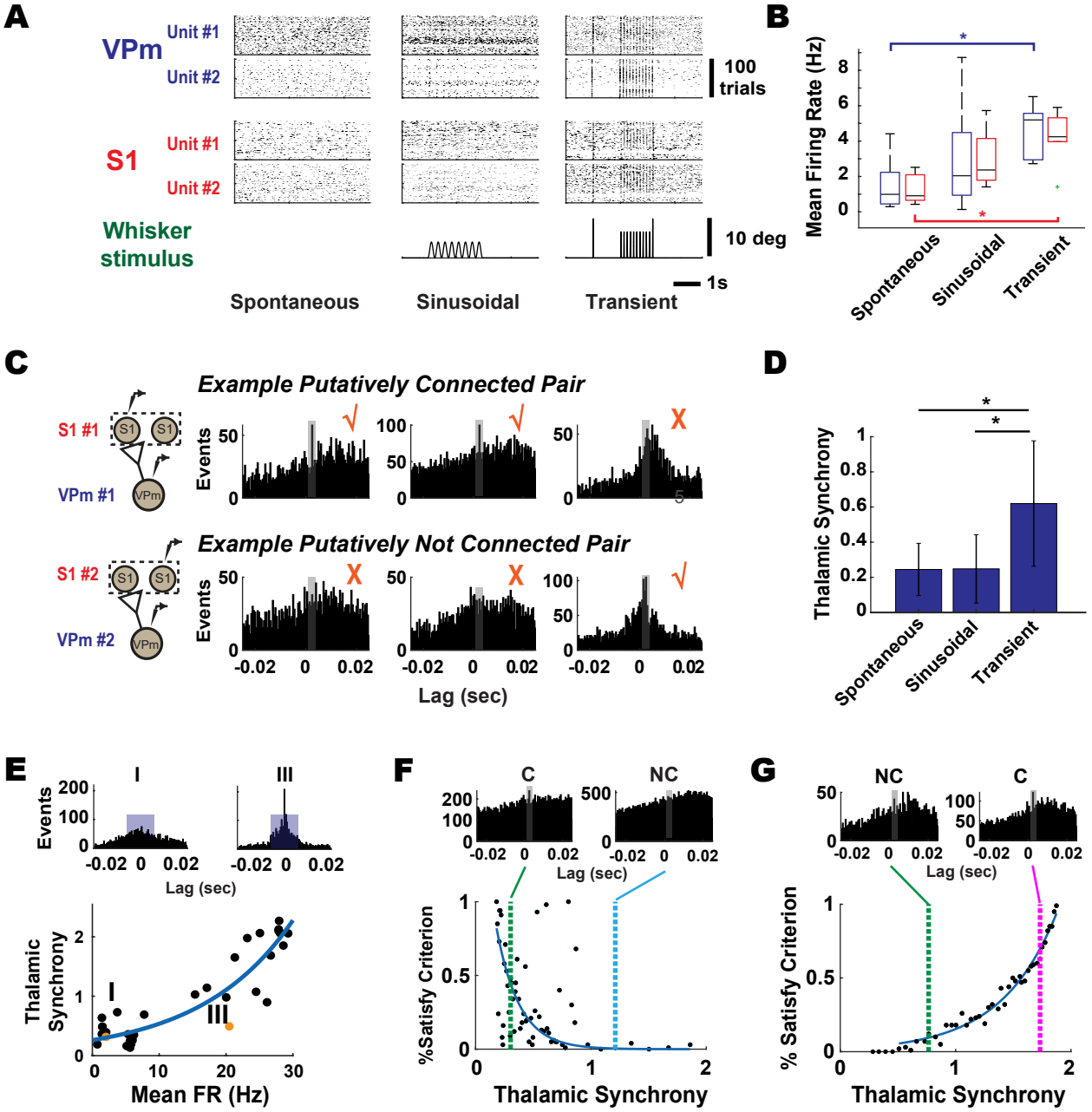
A
VPm
Unit #1
Unit #2
S1
Unit #1
Unit #2
Whisker stimulus
100 trials
10 deg
1s
Spontaneous
Sinusoidal
Transient
B
Mean Firing Rate (Hz)
Spontaneous
Sinusoidal
Transient
C
Example Putatively Connected Pair
S1 #1
VPm #1
Events
Example Putatively Not Connected Pair
S1 #2
VPm #2
Lag (sec)
D
Thalamic Synchrony
Spontaneous
Sinusoidal
Transient
E
I
III
Events
Lag (sec)
Thalamic Synchrony
Mean FR (Hz)
F
C
NC
Lag (sec)
%Satisfy Criterion
Thalamic Synchrony
G
NC
C
Lag (sec)
% Satisfy Criterion
Thalamic Synchrony

Figure 6

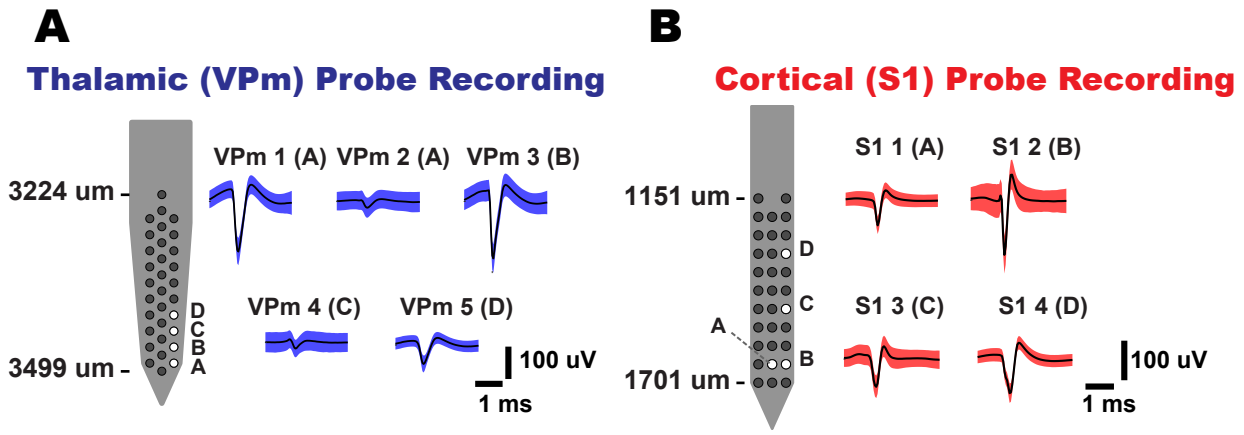

Table 1 Binary Classification					
	VPm 1	VPm 2	VPm 3	VPm 4	VPm 5
S1 1	NC	NC	NC	C	NC
S1 2	NC	C	NC	NC	NC
S1 3	NC	NC	NC	NC	NC
S1 4	NC	NC	NC	NC	C

Table 2 Probability of Correct Inference					
	VPm 1	VPm 2	VPm 3	VPm 4	VPm 5
S1 1	0.03	0.16	0.31	0.26	0.09
S1 2	0.06	0.80	0.15	0.09	0.09
S1 3	0.24	0.26	0.28	0.33	0.03
S1 4	0.28	0.14	0.10	0.22	0.67

Figure 7

Supplementary Figure 1

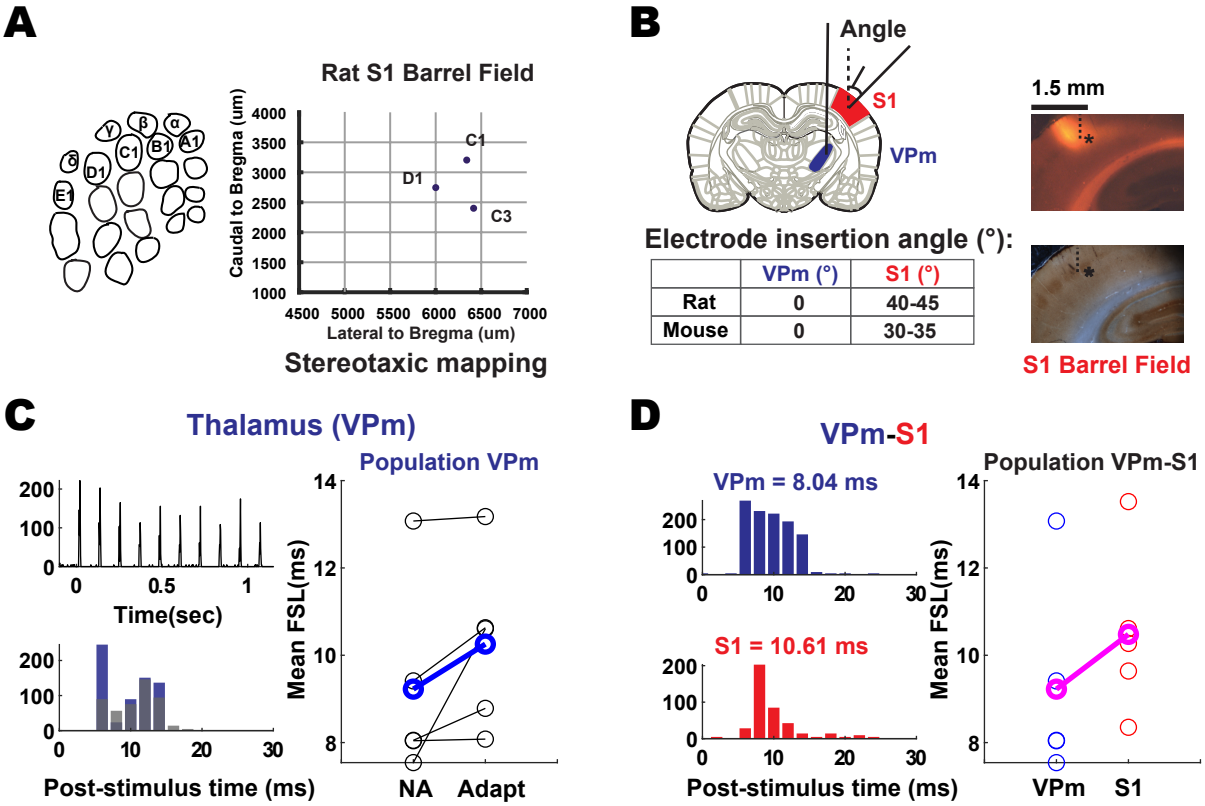

A. S1 targeting in rat (similar to main Figure 2A): Prior to actual recording, location of S1 barrels was determined using electrophysiology and stereotaxic coordinates using Bregma as a reference. We mapped three distinct locations of the barrels and fitted a barrel map template using the triangulation method. This functional map was later used to guide electrode placement for targeting a desired barrel column. **B.** (related to 2C). The optimal electrode insertion angle for targeting VPm and S1 in rat and mouse respectively. Histological images showing fluorescent electrode track (top) targeting S1 L4. **C.** Example adapting response of a single thalamic unit, showing mean first-spike latency in response to first and last pulse of a 8Hz pulsatile, ongoing stimulus (1st pulse: 9.41 ms, last pulse: 10.63 ms). (Right) Population adapting response for thalamic units (n=5 neurons, N = 1 mouse). Thick blue line showing mean first spike latency for first and last pulse of an 8Hz pulsatile, ongoing stimulus. All thalamic units that we recorded showed minimal latency shift (latency shift= 1.03 ± 1.24 ms, n = 5 neurons, N = 1 mouse), suggested that they were thalamic VPm units. **D.** (Left) Example peri-stimulus time histogram (PSTH, 1 ms binsize) for a thalamic and cortical unit in the 30-ms window following punctate (600°/s) whisker stimulus. We computed mean first spike latency (FSL), defined as average latency of first spike in 30 ms response window after stimulus presentation for each unit (VPm: 8.04 ms, S1: 10.61 ms). (Right) Population mean first spike latency for all simultaneously recorded thalamic and cortical units (VPm: 9.22 ± 2.26 ms, S1: 10.48 ± 1.26 ms, n = 5 pairs, N = 1 mouse). Thick purple line showed the mean first spike latency for each region.

Supplementary Figure 2

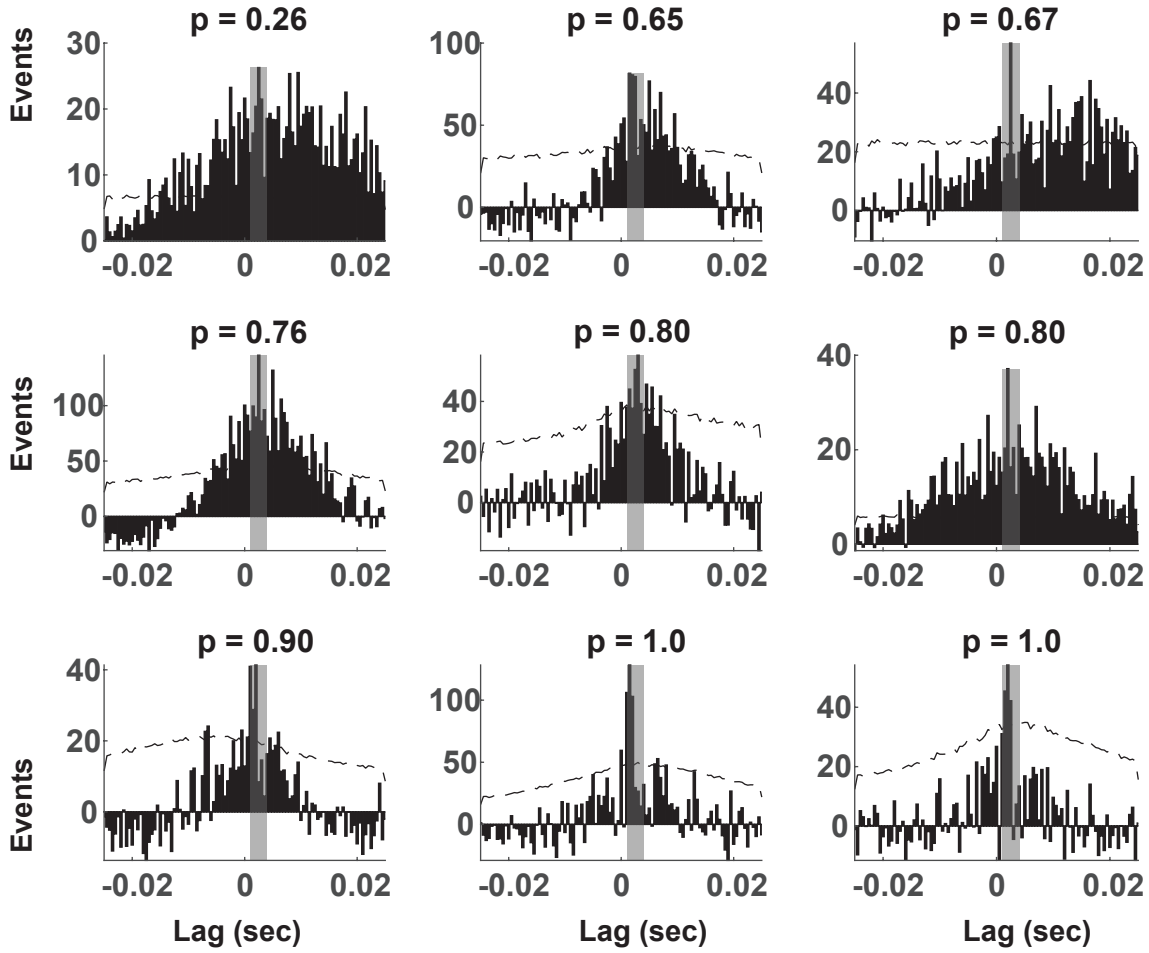

Shuffled-corrected cross-correlograms of all ‘connected’ pairs. P value above each plot represents the probability of a correct inference associated with each pair (related to Figure 4C and Figure 7 Table 2).